

Universität Bayreuth
Fakultät für Mathematik, Physik und Informatik
Lehrstuhl für Experimentalphysik X

Master Thesis

Colloidal edge currents between topologically equivalent lattices

submitted by

Adrian Ernst

Bayreuth, 26th February 2019

1. Assessor: Prof. Thomas M. Fischer
2. Assessor: Dr. Daniel de las Heras

Universität Bayreuth
Fakultät für Mathematik, Physik und Informatik
Lehrstuhl für Experimentalphysik X

Master Thesis

Colloidal edge currents between topologically equivalent lattices

submitted by

Adrian Ernst

Bayreuth, 26th February 2019

1. Assessor: Prof. Thomas M. Fischer
2. Assessor: Dr. Daniel de las Heras

Contents

1	Introduction	5
2	Pattern	7
3	Experimental setup	11
4	Mathematical Model	17
4.1	Pattern magnetic field	17
4.2	Particle potential	18
4.3	Stationary magnetic field	18
5	Simulations and loop generation	21
5.1	Calculation of particle potential	21
5.2	Brownian dynamics simulation	21
5.3	Four-fold pattern topology	23
5.4	Modulation loops	25
5.5	Ratchet detection in simulations	27
6	Results	29
6.1	Cyclotron loops	29
6.2	Asymmetric palindrome cyclotron loops	32
6.3	Symmetric palindrome cyclotron loops	37
6.4	Phasediagrams for palindrome loops	38
6.5	Behavioral modes	43
6.6	Symmetry considerations	49
6.7	Fences	50
7	Conclusions	55
8	Zusammenfassung	57
	Bibliography	59

1 Introduction

Colloidal particles have a huge area of application, so controlling their movement is crucial to tap their full potential. There are many different ways for doing this, for example using optical tweezers [1]. If we wanted to move many particles at the same time, it is possible to use thermal ratchets [2], as well as magnetic field gradients [3] or solute gradients [4]. Additional methods use direct propulsion of the particle, such as self-propulsion by chemical or thermal active particles [5, 6] or externally driven propulsion [7]. An other way is to use structured magnetic patterns which can be used to control magnetic particles [8]. Now being in control over such particles, one can use them as moving carriers in lab on a chip applications [9]. Furthermore, such systems can be used to model other physical systems, such as solid state bodies. An example are quantum edge states in topological insulators [10].

We work with micrometer-sized superparamagnetic core-shell particles on top of a magnetic 2-dimensional pattern, applying an external magnetic field with varying orientation. We can describe the resulting transport using topological invariants [11]. That means by winding the external magnetic field around certain points, we can derive the resulting motion. Topological transport can be shown using a variety of patterns, for example patterns having two-, three- or four-fold symmetric patterns [12]. Depending on the pattern, the particle movement can only show adiabatic movement where the particle stays always inside one minimum of its effective potential, or the minimum can annihilate with a saddle point and the particle is following the path of steepest descend what we call ratchet. Combining two of these patterns can show interesting effects like skipping orbits when combining a hexagonal lattice with a two-fold stripe lattice. Instead of varying the lattice symmetry, one can also try to combine equivalent lattices, only differing by their lattice constant [13].

In this thesis, we study two connected four-fold lattices having the same topological properties with different lattice constants, one double the other. This means for the particle potential, that the smaller lattice has double the amount of minima than the large lattice near the edge between the two simple patterns. Whereas we can observe only adiabatic transport in the bulk four-fold pattern, this leads to ratchet movements in some cases and we can then observe movements along the edge, whereas particles in the bulk in one of the lattices only perform trivial motion. We will explain the movements with simple symmetry based arguments and support this theory with results from experiments and simulations. The experiments are performed using paramagnetic colloidal particles on a thin magnetic pattern, driven by a modulated three-dimensional external magnetic field generated by coils. The simulations are done using Brownian Dynamics with the particle potential depending on the external magnetic field and the

1 Introduction

pattern magnetic field at the particle location. They will also be used to get information about the many different edge pattern variations, because our pattern definition allow the choice of three independent parameters. We will also show that the transport is topological and identify bifurcation points by varying the modulations of the external field in simulations and compare the resulting particle positions.

I did the experiments together with Helena Massana-Cid visiting Bayreuth from the University of Barcelona.

2 Pattern

A general four-fold pattern can be described by

$$P(a, \mathbf{x}_{\mathcal{A}}) = \text{sgn} \left[\cos \left(2\pi \frac{x_{1\mathcal{A}}}{a} \right) + \cos \left(2\pi \frac{x_{2\mathcal{A}}}{a} \right) \right] \quad (2.1)$$

where sgn is the sign function, a denotes the lattice constant and $\mathbf{x}_{\mathcal{A}} = (x_{1\mathcal{A}}, x_{2\mathcal{A}})$ the position in action space \mathcal{A} . P equals the \mathbf{e}_3 -direction of the magnetization $\mathbf{M} = PM\mathbf{e}_3$. The magnetization in \mathbf{e}_1 and \mathbf{e}_2 direction is zero. In figures, positive values of P are drawn white, negative values black. We now want to connect two of these lattices. Thus we define the new pattern piecewise as

$$P_e(a, \mathbf{x}_{\mathcal{A}}) = \begin{cases} P(a^{(1)}, \mathbf{x}_{\mathcal{A}} - \Delta\mathbf{x}_{\mathcal{A}}^{(1)}) & \text{if } x_{2\mathcal{A}} < 0 \\ P(a^{(2)}, \mathbf{x}_{\mathcal{A}} - \Delta\mathbf{x}_{\mathcal{A}}^{(2)}) & \text{else} \end{cases} \quad (2.2)$$

where $a^{(i)}$ and $\Delta\mathbf{x}_{\mathcal{A}}^{(i)}$ correspond to the bottom ($i = 1$) and top ($i = 2$) pattern. Changing $\Delta x_{1\mathcal{A}}^{(1)}$ and $\Delta x_{1\mathcal{A}}^{(2)}$ simultaneously shifts the pattern only by a global offset, so we can set $\Delta x_{1\mathcal{A}}^{(2)} = 0$ and have now three remaining scalar parameters to shift the two patterns relative to each other.

The pattern we are interested in has double the lattice constant for one pattern, that means $2a^{(1)} = a^{(2)} =: a$. We will call this pattern P_2 . For easier reading we rename the superscripts (1) and (2) to (s) and (l) for small and large patterns, see Figure 2.1. The periodicity of the parameters are summarized in Table 2.1. Furthermore we have mirror symmetric patterns for certain $\Delta x_{1\mathcal{A}}^{(s)}$. Both, the small and the large lattice, have their own symmetry plane. If we have a symmetric P_2 pattern, some symmetry planes from

parameter	periodicity
$\Delta x_{1\mathcal{A}}^{(s)}$	$\frac{a}{2}$
$\Delta x_{2\mathcal{A}}^{(s)}$	$\frac{a}{2}$
$\Delta x_{2\mathcal{A}}^{(l)}$	a

Table 2.1: Periodicities for pattern P_2

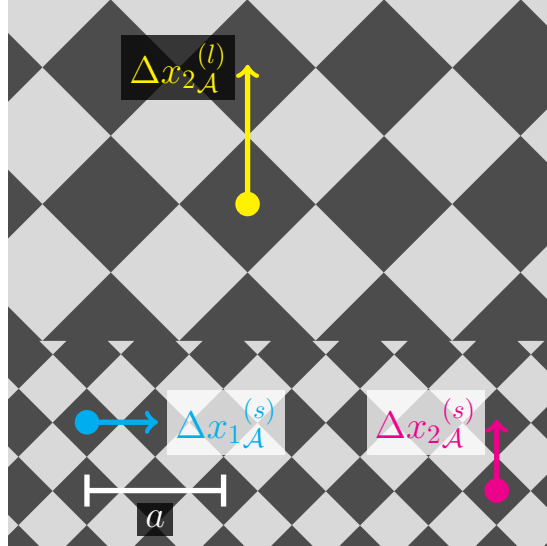


Figure 2.1: Shifting parameters for the P_2 pattern. The length of the arrows is the periodicity of the parameter.

both patterns coincide. This is the case if

$$\Delta x_{1\mathcal{A}}^{(s)} = n \frac{a}{4}, n \in \mathbb{Z}. \quad (2.3)$$

If n is even, there exist non-alternating symmetry planes running only through areas with $P > 0$, and through areas with $P < 0$ else, see Figure 2.2. There is a second type, the alternating symmetry plane running through areas with different P .

For other $\Delta x_{1\mathcal{A}}^{(s)}$ there is no common symmetry plane, but we can find a mirrored pattern by just changing $\Delta x_{1\mathcal{A}}^{(s)}$. A simple rule to find one of these patterns is to change the sign of $\Delta x_{1\mathcal{A}}^{(s)}$.

To get a pattern where white and black areas are exchanged, we have to add half of the periodicity size to each parameter:

$$\Delta x_{1\mathcal{A}}^{(s)'} = \Delta x_{1\mathcal{A}}^{(s)} + \frac{a}{4} \quad (2.4a)$$

$$\Delta x_{2\mathcal{A}}^{(s)'} = \Delta x_{2\mathcal{A}}^{(s)} + \frac{a}{4} \quad (2.4b)$$

$$\Delta x_{2\mathcal{A}}^{(l)'} = \Delta x_{2\mathcal{A}}^{(l)} + \frac{a}{2} \quad (2.4c)$$

The integral over the magnetization of the bulk pattern is zero, which means that the average magnetization of the pattern is zero because the areas with positive and negative magnetization have the same size. If we now introduce the edge in the P_2 pattern, this is not always the case any more. That means there is no general description possible

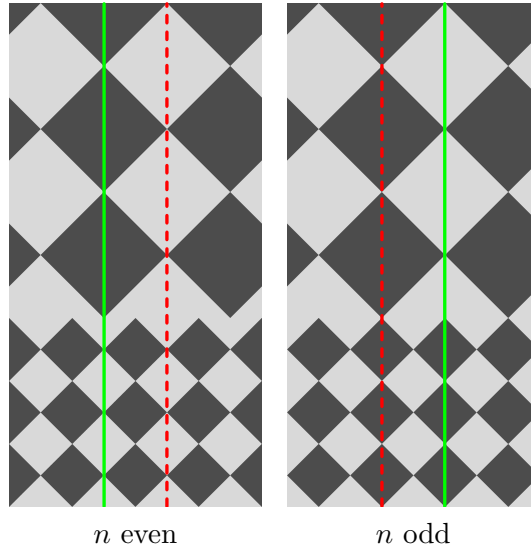


Figure 2.2: Non-alternating mirror planes for n odd and even according to Equation 2.3 are shown dashed in red, alternating mirror planes are shown in green.

and we have a non zero net magnetization of the whole pattern, which can be neglected because it adds only a constant factor to the particle potential.

3 Experimental setup

The experimental setup bases on a lithographic magnetic film with areas of different magentisations in shape of specific patterns. On top, paramagnetic colloidal particles move at a constant height driven by an external magnetic field, generated by coils. As the particle size is on a microscopic scale they are observed via light microscopy. By modulating the external magnetic field, the particles move in a plane parallel to the film. We call this plane where we do our observations action space \mathcal{A} . The external field direction is lying on a sphere that we call control space \mathcal{C} because it is used to control the particles. An overview of the experiment is given in Figure 3.1.

Below are the details of the setup used for all experiments.

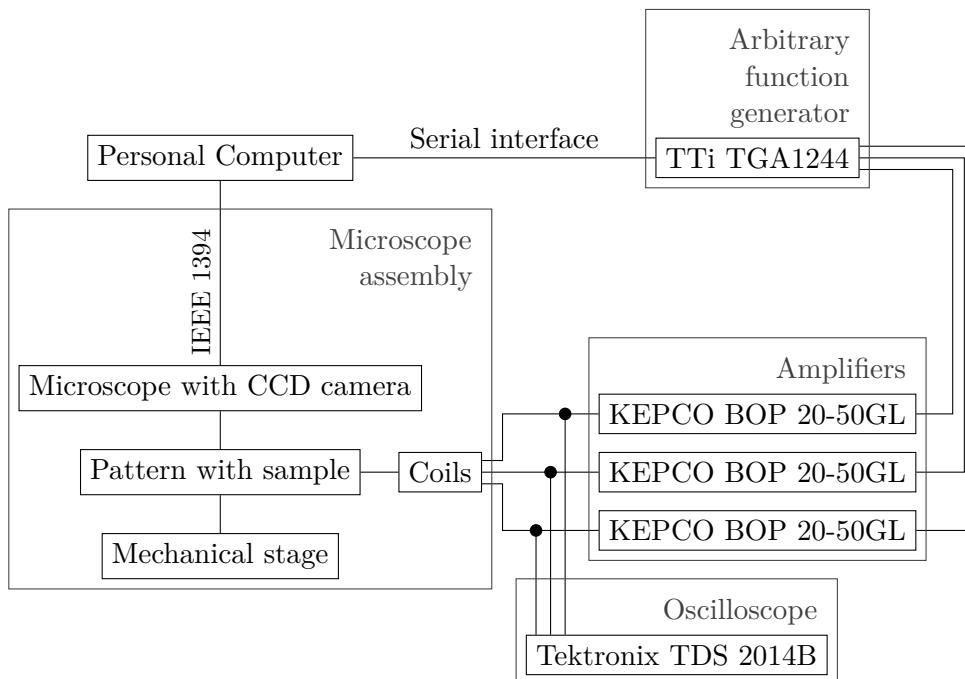


Figure 3.1: Schematic of the setup used for the experiments.

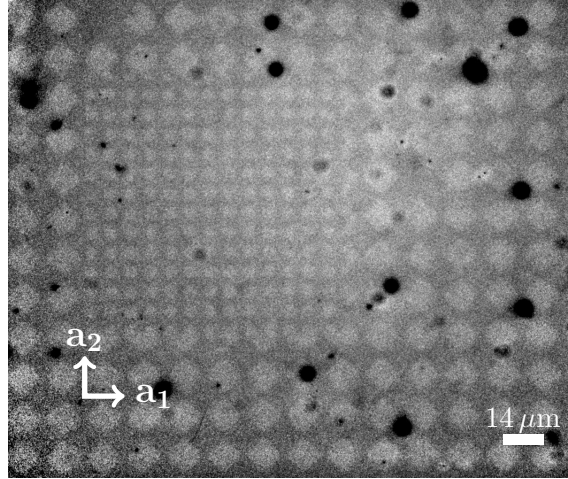


Figure 3.2: Microscopy image of the pattern with the lattice vectors \mathbf{a}_1 and \mathbf{a}_2 . Colloids appear as black circles.

Magnetic lithographic film

The magnetic lithographic film was produced in cooperation with the Institute of Physics and Centre for Interdisciplinary Nanostructure Science Technology in Kassel as well as the Institute of Molecular Physics in Poznań (Poland) [14–16]. It is based on the multi-layer system $\text{Ti}^{4\text{nm}}/\text{Au}^{60\text{nm}}/[\text{Co}^{0.7\text{nm}}/\text{Au}^{1\text{nm}}]^5$ on a silicon substrate. Subsequently it was covered with a shadow mask created by UV lithography with a chromium hard mask providing the structure of the pattern. Subsequently He-ion bombardment led to a decrease of the coercive field of the pattern in the uncovered areas. The resulting magnetic layer has a thickness of 3.5 nm. Brighter looking areas are magnetized in the direction of the surface normal, darker areas in the opposite direction.

To keep the colloidal particles at a certain height above the pattern, it was spin-coated with *MicroChemicals AZ 1512HS* positive photoresist at 3000 rpm to create a $1.6 \mu\text{m}$ polymer film.

Square patterns with edge

We use a pattern with an edge between two four-fold patterns with lattice constants $a = 14 \mu\text{m}$ and $\frac{a}{2} = 7 \mu\text{m}$. The pattern with the small lattice constant is enclosed by the lattice with the large lattice constant. They are arranged in a way we have access to four different types of edges. The edges are running parallel to the lattice vectors a_1 or a_2 , see Figure 3.2.

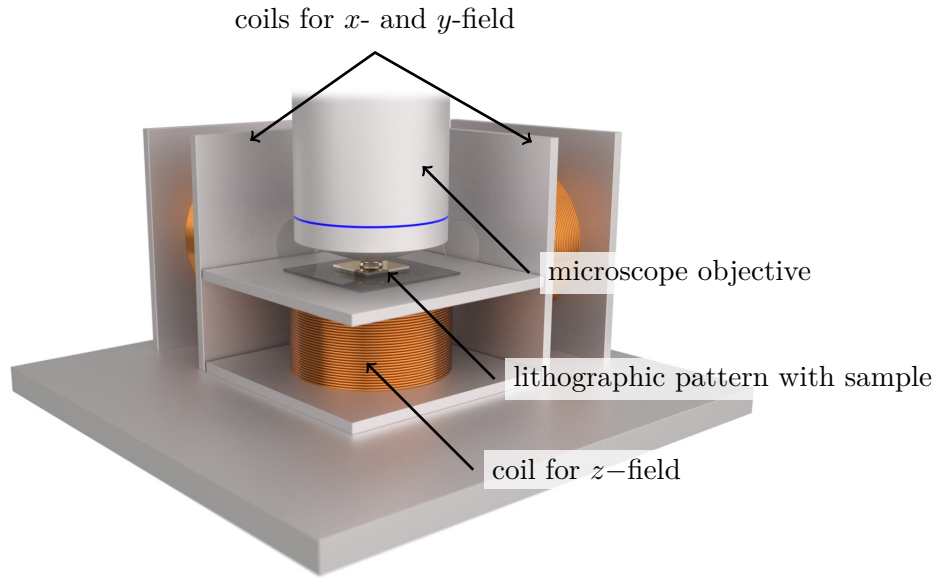


Figure 3.3: Three coils generating the external magnetic field and the lithographic pattern with the immersed microscope objective.

External field creation

The external field to drive the particles on top of the pattern is generated by three cylindrical copper coils with their center axis perpendicular to each other as shown in Figure 3.3. Above the center of the coil for the vertical component of the field, we position the lithographic film on a microscope glass slide. The other coils are arranged such that their rotational axis passes through the region of interest. This is necessary to keep the x-, y- and z-components of the magnetic field perpendicular for getting the desired external field. As the length scale ($\approx 14 \mu\text{m}$) of one unit cell is very small against the diameter of the coils (15 mm), we can assume the magnetic field being constant. The loops are generated on the PC according to the parameters in section 5.4 “Modulation loops”. They are then converted into the three field components such that the total magnetic field strength is constant. Via a serial connection these are transferred to the arbitrary function generator *TTi TGA1244* (Figure 3.5), which is used to generate the waveforms for the three coils. The generator output is amplified by three amplifiers of type *KEPCO BOP 20-50GL* to drive the low resistance coils. To check the signal, an oscilloscope (*Tektronix TDS 2014B*) is used. The resulting magnetic field is approximately $10 \frac{\text{kA}}{\text{m}}$. It was calibrated for each of the three coils by adjusting the waveform generator output voltage to get the desired field, measured by a *Lake Shore 410* Gaussmeter.

3 Experimental setup



Figure 3.4: Image of the microscope used with coils for external magnetic field creation.

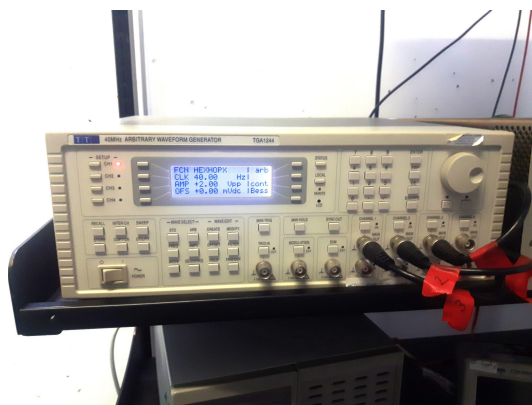


Figure 3.5: Image of the arbitrary function generator used to generate the waveforms for the three coils.

Microscope

We use a *Leica DM2500P* microscope with the objective (*Leica C PLAN 63x/0.75*) immersed into the sample (Figure 3.4). We use top lighting because the lithographic film is opaque. The image is captured via a monochrome CCD camera (*Leica DFC360 FX*) and transferred to a computer for observation and recording. The pixel density of the resulting image has been determined as $5.35 \pm 0.05 \frac{\text{px}}{\mu\text{m}}$. The sample can be moved in horizontal directions using the mechanical stage.

Sample

The sample containing the paramagnetic colloidal particles is prepared by mixing purified water with *Dynabeads M-270* in a ratio of 4000:1. This is resulting in approximately 500 particles per μl . The resulting sample is mixed using a vortex mixer. We pipette $20 \mu\text{l}$ on the cleaned pattern film and wait until the particles have sedimented to the polymer film. Their center of mass is now approximately $3 \mu\text{m}$ above the magnetic pattern. Now the particles can be positioned using modulation loops of the external field and the experiments can be done.

Problems

As the particles have a dipole moment higher than the pattern if the external field is enabled, they attract each other. This is unwanted in our case because multiple connected colloids behave differently. Thus we have to reduce the concentration such that we have still enough particles in the areas where we want to do our experiments, but as less agglomeration as possible.

Another problem in the experiments is that the pattern has experienced damage such as scratches from previous experiments and cleaning, so colloids are often blocked at such defects and sometimes trapped. Sometimes they can be freed again by applying different modulated external fields, but often they can not be recovered and are lost for use in the experiment.

4 Mathematical Model

The system consisting of the thin magnetic pattern and the paramagnetic particles can be described by a simple mathematical model. We first derive the magnetic field of the pattern at a certain height above it and then the potential of the particle inside that field. Based on this we explain some properties of that potential which are useful for understanding the movement of the colloidal particles.

4.1 Pattern magnetic field

The magnetic pattern consists of different regions with magnetisations $\mathbf{M}(\mathbf{x}_A) = M(\mathbf{x}_A) \mathbf{e}_3$ in the x_{1A} - x_{2A} -plane (action space \mathcal{A}). The magnetic field of the pattern can be expressed by Poisson's equation [17]

$$\Delta \Psi = \nabla \cdot \mathbf{M} \quad (4.1)$$

where Ψ is the magnetic potential given by

$$\mathbf{H}_P = -\nabla \Psi \quad (4.2)$$

with \mathbf{H}_P the magnetic field of the pattern. The Green's function of the Laplace operator

$$G_\Delta(\mathbf{x}) = -\frac{1}{4\pi} \frac{1}{|\mathbf{x}|} \quad (4.3)$$

solves the Poisson's equation and gives us the magnetic potential

$$\Psi(\mathbf{x}) = \int_V d^3 \mathbf{x}' G_\Delta(\mathbf{x} - \mathbf{x}') \nabla_{\mathbf{x}'} \cdot \mathbf{M}(\mathbf{x}') \quad (4.4)$$

and thus the magnetic field

$$\mathbf{H}_P(\mathbf{x}) = \nabla_{\mathbf{x}} \int_V d^3 \mathbf{x}' \frac{\nabla_{\mathbf{x}'} \cdot \mathbf{M}(\mathbf{x}')}{4\pi |\mathbf{x} - \mathbf{x}'|} \quad (4.5)$$

Assuming a thin film at $x_3 = 0$ we can set $\nabla_{\mathbf{x}} \cdot \mathbf{M}(\mathbf{x}) = M(\mathbf{x}_A) \delta(x_3)$. The magnetic field is now

$$\mathbf{H}_P(\mathbf{x}_A, z) = \int_{\mathcal{A}} d^2 \mathbf{x}'_A \frac{(\mathbf{x}_A - \mathbf{x}'_A) + z \mathbf{e}_3}{4\pi |(\mathbf{x}_A - \mathbf{x}'_A) + z \mathbf{e}_3|^3} M(\mathbf{x}'_A) \quad (4.6)$$

integrating over the $x_{1\mathcal{A}}-x_{2\mathcal{A}}$ -plane which equals the action space \mathcal{A} , and z is the height above the pattern, see Figure 4.1a for an example.

4.2 Particle potential

Now we can derive the potential of our colloids above the pattern with a constant external magnetic field \mathbf{H}_{ext} . The magnetic moments \mathbf{m} of the colloids with volume V and a relative susceptibility χ_{eff} are induced by the magnetic field \mathbf{H} :

$$\mathbf{m} = \chi_{eff}V\mathbf{H} \quad (4.7)$$

The energy of one particle can then be written as

$$E = -\mu_0\mathbf{m} \cdot \mathbf{H} = -\mu_0\chi_{eff}V\mathbf{H}^2 \quad (4.8)$$

which leads to a particle potential

$$U \propto -\mathbf{H}^2 = -(\mathbf{H}_P + \mathbf{H}_{ext})^2. \quad (4.9)$$

As the shape of the potential landscape changes only with the direction of \mathbf{H}_{ext} , but not with its absolute value, we can restrict \mathbf{H}_{ext} to a constant length, thus lying on a sphere. This sphere of the external field is called control space \mathcal{C} as it is used to control the particle potential. We can now describe \mathbf{H}_{ext} by two polar coordinates θ and ϕ . The conversion to Cartesian coordinates is defined by:

$$\begin{aligned} x_1 &= \cos(\phi) \sin(\theta) \\ x_2 &= \sin(\phi) \sin(\theta) \\ x_3 &= \cos(\theta) \end{aligned} \quad (4.10)$$

Because the colloids are far away from the magnetic pattern such that \mathbf{H}_P^2 is small and \mathbf{H}_{ext}^2 is now constant, the potential can be approximated by

$$U(\mathbf{x}_{\mathcal{A}}, \mathbf{H}_{ext}) \approx -\mathbf{H}_P(\mathbf{x}_{\mathcal{A}}) \cdot \mathbf{H}_{ext}. \quad (4.11)$$

A plot of the resulting potential for an example \mathbf{H}_{ext} and P_2 pattern is shown in Figure 4.1b.

4.3 Stationary magnetic field

For a given \mathbf{H}_{ext} we have minima, maxima and saddle points of the potential U in action space. Because U can be written as a scalar product of \mathbf{H}_P and \mathbf{H}_{ext} , changing $\mathbf{H}_{ext} \rightarrow -\mathbf{H}_{ext}$ converts all minima to maxima and vice versa. We call the regions where minima respective maxima can be located for any \mathbf{H}_{ext} allowed regions, the others

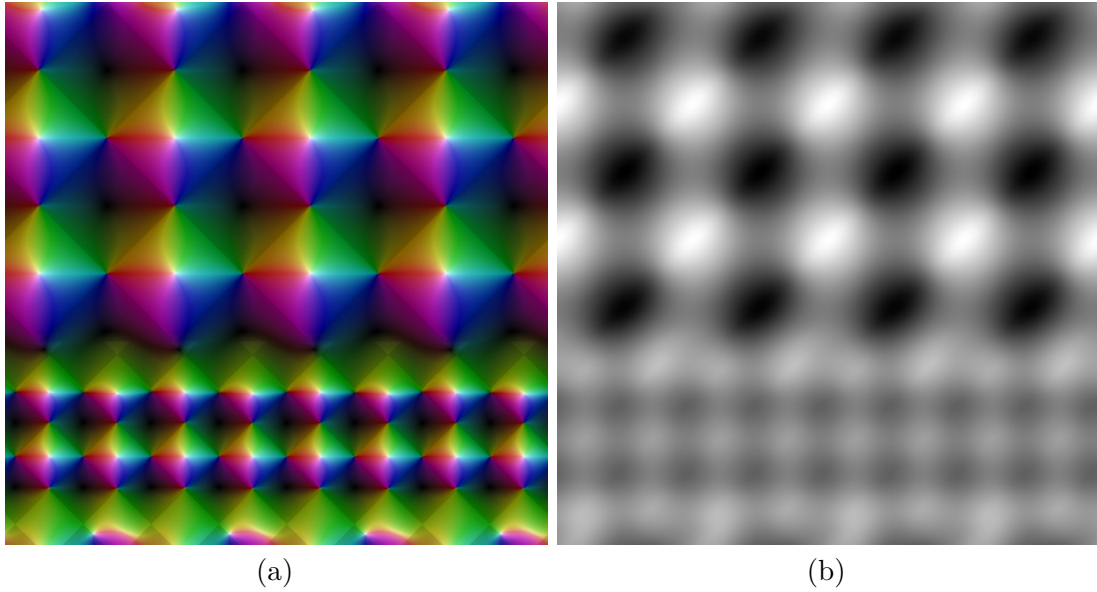


Figure 4.1: Examples of magnetic field and particle potential for a P_2 pattern; (a) shows the \mathbf{H} field at a fixed height, overlaid with the black and white pattern image. The colors indicate the direction in the x_1 - x_2 -plane and the brightness the x_3 -component of the field; (b) shows the corresponding paramagnetic particle potential for $\mathbf{H}_{ext} = (1, -1, 0)$ with the brightness proportional to the potential value, such that the particle is located in the dark areas. As you can see, the part of the pattern with the small lattice constant has double as many minima along the edge as the large pattern.

4 Mathematical Model

forbidden regions. In allowed regions, adiabatic transport is possible, whereas the particle can be found in forbidden regions only temporary while in a ratchet movement, following the path of steepest descent to a minimum. A point \mathbf{x}_A is such a stationary point of U if the external field is stationary:

$$\mathbf{H}_{ext}^s(\mathbf{x}_A) \propto \pm \partial_{x_1} \mathbf{H}_P(\mathbf{x}_A) \times \partial_{x_2} \mathbf{H}_P(\mathbf{x}_A). \quad (4.12)$$

Using this external field we can test for allowed and forbidden regions by using the determinant of the Hessian matrix:

$$|\mathbf{H}_{ext}^s(\mathbf{x}_A) \cdot \nabla_A \nabla_A \mathbf{H}_P(\mathbf{x}_A)| \begin{cases} > 0 & : \text{allowed region, extremum} \\ < 0 & : \text{forbidden region, saddle point} \end{cases} \quad (4.13)$$

It is further possible to split the allowed regions into north and south allowed regions. North (south) regions are regions where a minimum exists if $\mathbf{H}_{ext,3}^s$ is positive (negative).

By modulating the external field \mathbf{H}_{ext} , the positions of minima change. That means a particle is moving along with the minimum it is located in. This motion is time reversible, i.e. reversing the modulation moves the particle the same way back without hysteresis. We call that an adiabatic motion.

In contrast, if a minimum passes the border of the allowed region, the fence, it meets a saddle point from the forbidden region and annihilate. As the particle is not a stable position any more, it moves along the path of steepest descend to another minimum. This movement is called a ratchet motion. A ratchet motion is not time reversible and cannot be easily predicted, even if knowing the position of all minima.

5 Simulations and loop generation

The mathematical model described before can be used to simulate the behavior of the colloids for arbitrary magnetic patterns. This is done using Brownian dynamics simulations which neglects the inertia of the particle, similar to the real system. In addition, we use random numbers to introduce noise in the simulation to prevent that particles stay at saddle points or maxima of the particle potential. In this chapter we will discuss the details of the simulations and how the loops for the experiments are generated.

5.1 Calculation of particle potential

The pattern is generated on a pixel (px) grid. This is used to calculate the pattern's magnetic field \mathbf{H}_{ext} on the same grid using Equation 4.6 with the height $z = 0.2a$ above the pattern. The integration of $\mathbf{H}_{ext}(\mathbf{x})$ is performed over a circular area around \mathbf{x} with radius r . This is possible, because the sum of magnetic moments of one full unit cell is zero, and for large r the sum of contributions of the cells cut by the integration circle is small. We calculated the potential of one point for different r to find a good value for the radius, see Figure 5.1. The resulting pattern field is filtered using a Gaussian filter with a standard deviation of $\sigma = 3$ px to remove artifacts created by the numeric integration.

5.2 Brownian dynamics simulation

The simulations are done using Brownian dynamics simulations. A paramagnetic particle moves at a fixed height z , driven by the potential gradient force \mathbf{F}_{pg} and a random force \mathbf{F}_B , both damped by a friction factor ξ . The equation of motion can then be written as

$$\xi \dot{\mathbf{x}}_A = \mathbf{F}_{pg} + \mathbf{F}_B \quad (5.1)$$

We use two timescales, one for the integration of the equation of motion of the particle $T_I = 1$ step, and one for the change of the external field $T_F = 1000 T_I$. For a loop in control space with $n = 1000$ points, the number of integration steps is $n \cdot T_F = 10^6$ steps.

The gradient force is calculated numerically by calculating the symmetric difference

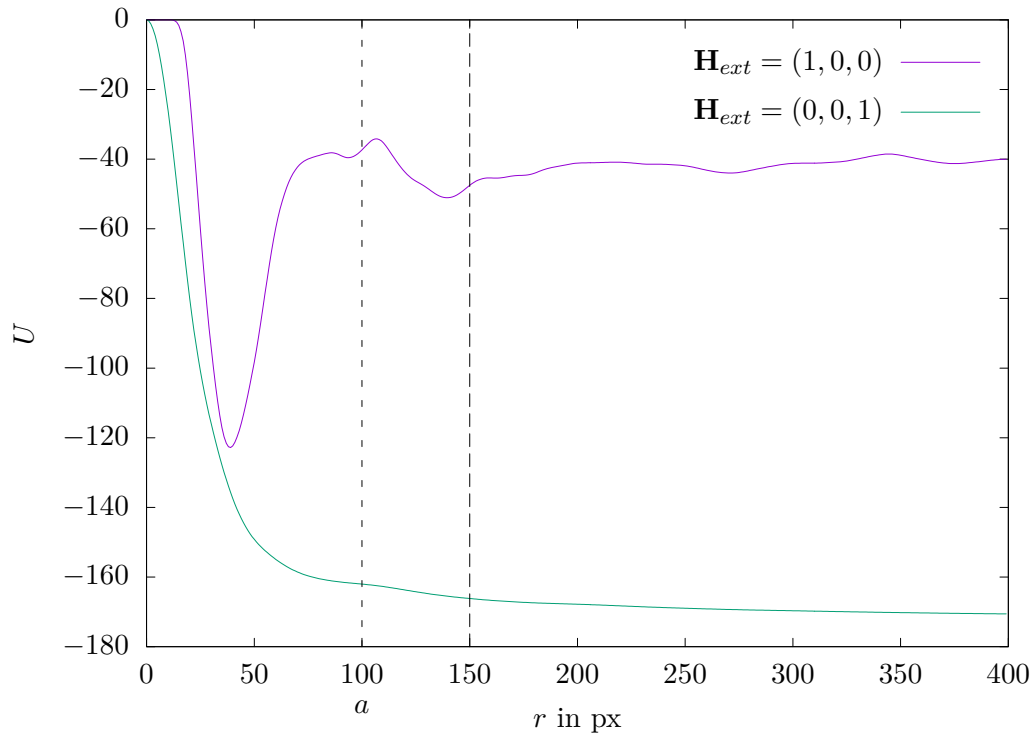


Figure 5.1: Potential values of one point directly at the edge for a P_2 four-fold edge pattern with lattice constant $a = 100px$, plotted for different integration radius values r for a given \mathbf{H}_{ext} . We see that U stabilizes after passing a value of $r \approx 150$ px.

quotient

$$(\mathbf{F}_{pg})_i = (-\nabla_{\mathbf{x}}U)_i = -\frac{U(\mathbf{x} + \mathbf{h}_i) - U(\mathbf{x} - \mathbf{h}_i)}{2h} \quad (5.2)$$

with $\mathbf{h} = (h, h, 0)$ and U the potential from Equation 4.11 for the given external field from the control space loop. As the potential value is available only on the grid \mathbf{H}_P has been calculated, h is a grid index step of one.

The random force \mathbf{F}_B is Gaussian distributed and calculated for every time step by using the Box-Muller transform based on random floating point numbers generated by a Mersenne-Twister generator [18]. First, we generate two pseudorandom floating point numbers u_1, u_2 in the interval $[0, 1)$. Then we apply the Box-Muller transform and scale the result with the standard deviation σ :

$$\mathbf{F}_B = \begin{pmatrix} \sigma\sqrt{-2\ln u_1} \cos(2\pi u_2) \\ \sigma\sqrt{-2\ln u_1} \sin(2\pi u_2) \end{pmatrix} \quad (5.3)$$

The standard deviation is chosen as $\sigma = 0.4a$, the friction constant as $\xi = 390\frac{M_z}{a}$. In x_3 -direction both forces are zero.

Finally, the equation of motion is integrated using Euler integration:

$$\mathbf{x}_A(t + T_I) = \mathbf{x}_A(t) + \frac{\mathbf{F}_{pg}(\mathbf{x}_A(t), t) + \mathbf{F}_B(t)}{\xi} T_I \quad (5.4)$$

5.3 Four-fold pattern topology

To have an idea how we design our loops to use with the four-fold edge patterns, we first take a look at the loops we would use for the bulk four-fold pattern. This pattern consists out of a lattice of squares with alternating positive and negative magnetisations, see Figure 5.2a. For external fields parallel or antiparallel to the surface normal vector, a paramagnetic particle is located in the center of the square with positive or negative magnetization. We now want to explain the transition between these two points. Calculating the allowed and forbidden regions as described before in section 4.3, we can see the fences crossing at four points for every unit cell. These gates are the only points where a minimum can exit its square, that is where a particle can exit adiabatically. Because of the $\pm x_3$ symmetry, these gates need to be at the equator ($\theta = 90^\circ$). You can see the gates in Figure 5.2b for action space \mathcal{A} and in Figure 5.3b for control space \mathcal{C} . In \mathcal{C} the four fences are just points at the equator with the gates between them. Winding around one fence point moves the particle one unit cell in a certain direction [19]. Details are given in Figure 5.3a. We will assume that the transport across and along the edge is similar to the bulk transport so we will use the same loops as for the bulk four-fold pattern.

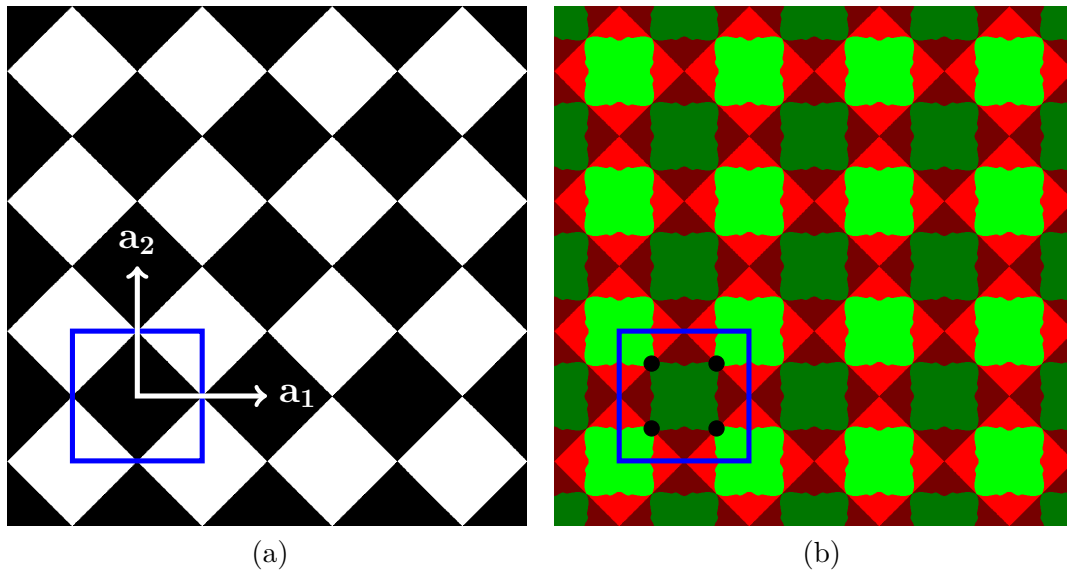


Figure 5.2: (a) Plot of the action space \mathcal{A} of a four-fold pattern. One unit cell is enclosed by a blue frame. White areas have positive, black areas have negative magnetization; (b) Corresponding forbidden (red) and allowed (green) regions in \mathcal{A} combined with the pattern. The allowed regions are in the center of the black and white areas, and the gates are marked as black points in the center of the boundaries between both. Fences are the borders between red and green regions.

5.4 Modulation loops

The modulation loops used in the simulation and the experiments are rectangular in θ - ϕ -space. They can be specified by a center point (θ_0, ϕ_0) and by the maximum displacement $(\Delta\theta, \Delta\phi)$ for each angle. Additionally, they can run in a mathematically positive or negative sense and can have different starting points.

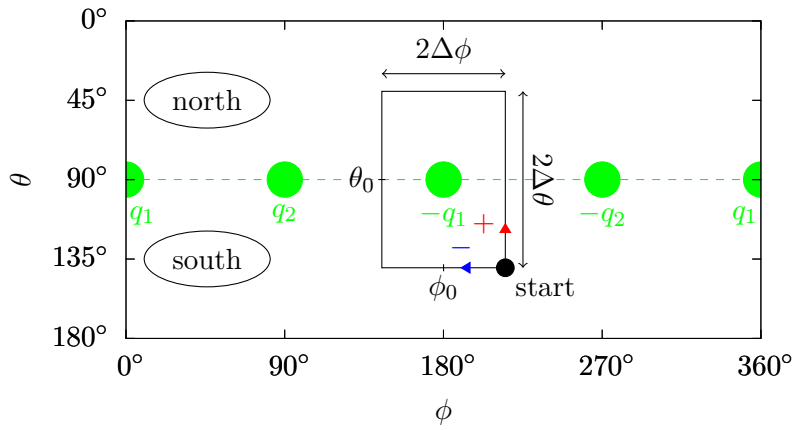
For the four-fold pattern there are 4 fence points to wind around. Thus we have a set of four (θ_0, ϕ_0) to use if we want to wind only around one point each, see Figure 5.3. For simplification we set $\Delta\theta = 90^\circ$ so we can connect multiple loops without worrying about the change from the end of one loop to the start of the next one. A loop is then described by three parameters, the winding point q , the ϕ -displacement $\Delta\phi$ and the number of windings n . We denote such a fundamental loop as $\mathcal{L}_q^n[\Delta\phi]$. If n is positive (negative), we wind around the fence point in mathematically positive (negative) sense. The time inverse of such a fundamental loop is written as $\mathcal{L}_q^{-n}[\Delta\phi]$. The starting point and end point is set at $(\theta_0 + \Delta\theta, \phi_0 + \Delta\phi)$, which is in the south, so the particle starts on a black area.

We can concatenate multiple of these fundamental loops to create a modulation that doesn't lead to net transport for the bulk four-fold pattern. The simplest way of doing that is to connect four loops winding around a different fence point each in the same sense. An example would be $\mathcal{L}_{q_1}^1 \mathcal{L}_{q_2}^1 \mathcal{L}_{-q_1}^1 \mathcal{L}_{-q_2}^1$. Additionally, we can create loops which are time reversible, that means they are identical in control space \mathcal{C} if you run them backwards. We can achieve that by extending the loop with its mirror image in a temporal sense. Using the example above gives us $\mathcal{L}_{q_1}^1 \mathcal{L}_{q_2}^1 \mathcal{L}_{-q_1}^1 \mathcal{L}_{-q_2}^1 \mathcal{L}_{-q_2}^{-1} \mathcal{L}_{-q_1}^{-1} \mathcal{L}_{q_2}^{-1} \mathcal{L}_{q_1}^{-1}$. We will call such loops palindrome loops.

If we now exchange the four-fold pattern with the four-fold edge pattern P_2 , the particle does generally not return to its start position. That leads to a net transport, which is parallel to the edge. We take a closer look at this transport in the next chapter.

fence point in \mathcal{C}	ϕ_0	direction in \mathcal{A}
q_1	0°	$-\mathbf{a}_2$
q_2	90°	\mathbf{a}_1
$-q_1$	180°	\mathbf{a}_2
$-q_2$	270°	$-\mathbf{a}_1$

(a)



(b)

Figure 5.3: Fence points for four-fold pattern: (a) lists the fence points and the corresponding ϕ in control space \mathcal{C} and the movement direction in action space \mathcal{A} ; (b) shows the fence points in \mathcal{C} projected into the ϕ - θ -plane as green circles and gates as green dashed lines. The red (blue) arrow indicates winding in mathematically positive (negative) sense around one fence point. The point for starting on an area with magnetization in $-\mathbf{e}_3$ -direction is marked with ‘start’.

5.5 Ratchet detection in simulations

To detect ratchets we can use the speed of the particle. For adiabatic movement the speed is proportional to the speed of the external field, for ratchets the speed is independent of it. If we now lower the speed of the external field by increasing the loop's timescale T_F relative to the integration timescale T_I , ratchets get visible as peaks as the speed for adiabatic movements gets smaller. Because of the noise introduced by the random force, we have to filter the positions or speed before use. The filtering is done using a Gaussian filter. Plotting the speed in action or in control space enables us to see points where ratchets occur, which are lying on fences, because there the minimum vanishes which leads to the ratchet.

To build a full fence diagram, we simulate loops with increasing $\Delta\phi$ hitting both poles. We wind around the two fence points for the bulk lattice q_1 and $-q_1$. Then we plot the speed for any of these loops in a ϕ - θ -diagram and the passed fences get visible as lines. This method only finds fences actually crossed by the used loops, not all of them. An alternative way of obtaining the fence is by calculating the forbidden and allowed regions as described in section 4.3 and finding the interface between both, which is also the fence. By calculating the stationary external field \mathbf{H}_{ext}^s there, we can also obtain the fence in control space \mathcal{C} .

6 Results

We used simulations and experiments with colloids on a magnetic pattern as described in the previous chapters. Looking at loops providing no net transport in the bulk, we found the existence of edge currents in the case of the particles passing the edge. In the following we will derive a theory based on basic symmetry considerations and verify it with experiments and simulation results.

6.1 Cyclotron loops

We start by running a simple modulation loop $\mathcal{L}_{-q_1}^{-n} \mathcal{L}_{-q_2}^{-n} \mathcal{L}_{-q_1}^n \mathcal{L}_{-q_2}^n$, $n = 2$ on a simple four-fold pattern with no edge. That means winding around two fence points of the four-fold lattice two times in each sense. This loop lets the particle move two unit cells in each of the main directions parallel or antiparallel to \mathbf{a}_1 or \mathbf{a}_2 as shown in Figure 6.1. That obviously leads to no net movement after one full modulation. We can also note that this is true for any $n \in \mathbb{Z}$. For this and all following loops in experiments and simulations we used $\Delta\phi = 35^\circ$, unless otherwise stated.

Next we use a P_2 pattern containing an edge and run again the same modulation $\mathcal{L}_{-q_1}^{-n} \mathcal{L}_{-q_2}^{-n} \mathcal{L}_{-q_1}^n \mathcal{L}_{-q_2}^n$, $n = 2$. The starting point lies on the large pattern and is selected such that the particle crosses the edge and the particle movements parallel to the edge are not influenced by it. Instead of no movement in the case of a simple four-fold pattern, on P_2 we observe that after one full modulation the particle is at a different location than at start, an edge transport has occurred. The particle is moving one large unit cell. This can be explained by decomposing the full loop into sub-loops, shown in different colors in Figure 6.2. The first and third part $\mathcal{L}_{-q_1}^{-2}$ (green) and $\mathcal{L}_{-q_1}^2$ (green) are both crossing the edge. The second part $\mathcal{L}_{-q_2}^{-2}$ (blue) moves the particle by a , which is the periodicity of the P_2 pattern in \mathbf{a}_1 direction. Thus the first subloop $\mathcal{L}_{-q_1}^{-2}$ (green) is fully reversed by the third one $\mathcal{L}_{-q_1}^2$ (green) because both are adiabatic and run at equal positions only separated by one large unit cell. This leads to no net movement. So the movement rises from the other two contributions. The second contribution $\mathcal{L}_{-q_2}^{-2}$ (blue) induces movement of a in \mathbf{a}_1 direction, the fourth part $\mathcal{L}_{-q_2}^2$ (blue) of $-2a$ in \mathbf{a}_1 direction. So the total displacement is $-a$ which is the size of one large unit cell, matching the result. For another cyclotron loop, the particle moves in the other direction if the direction of the second and fourth contributions are exchanged. We can calculate the total displacement s along \mathbf{a}_1 for one full modulation as

$$s(n) = \pm \frac{n}{2} \cdot a \quad (6.1)$$

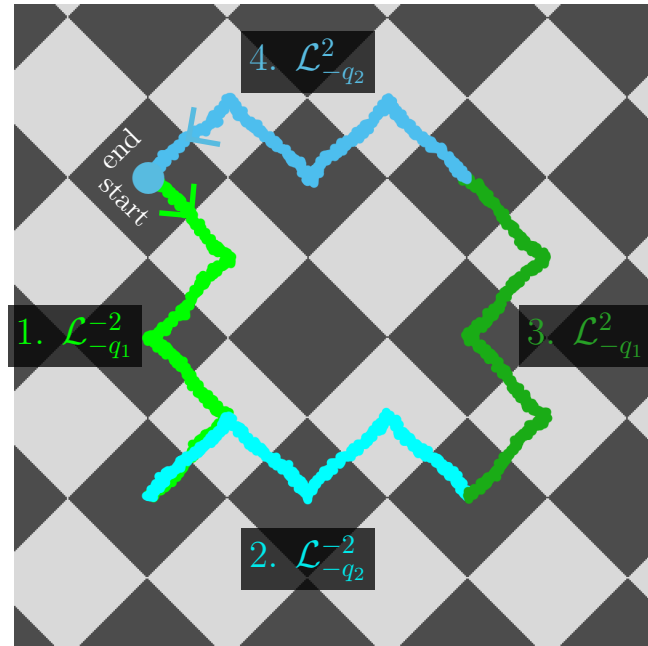


Figure 6.1: Even ($n = 2$) cyclotron loop $\mathcal{L}_{-q_1}^{-2} \mathcal{L}_{-q_2}^{-2} \mathcal{L}_{-q_1}^2 \mathcal{L}_{-q_2}^2$ on a simple four-fold pattern winding around two fence points. The trajectory was obtained using simulations.

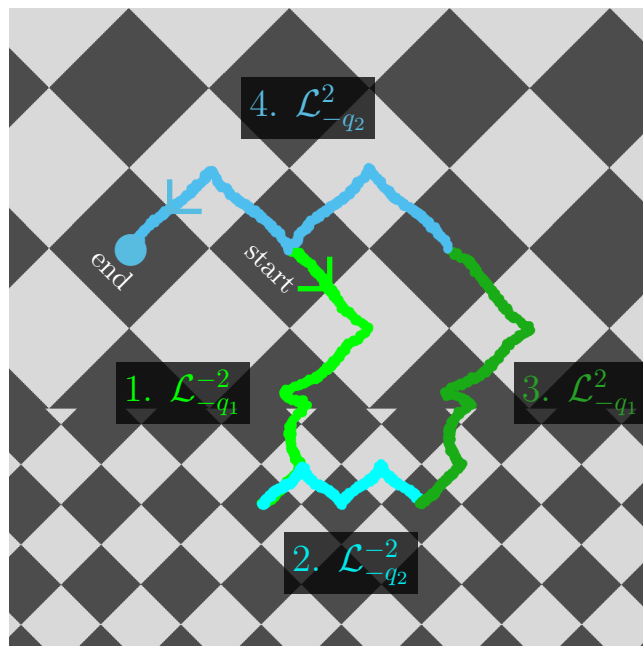


Figure 6.2: Even ($n = 2$) cyclotron loop $\mathcal{L}_{-q_1}^{-2} \mathcal{L}_{-q_2}^{-2} \mathcal{L}_{-q_1}^2 \mathcal{L}_{-q_2}^2$ on a P_2 four-fold edge pattern using two fence points, trajectory from simulations.

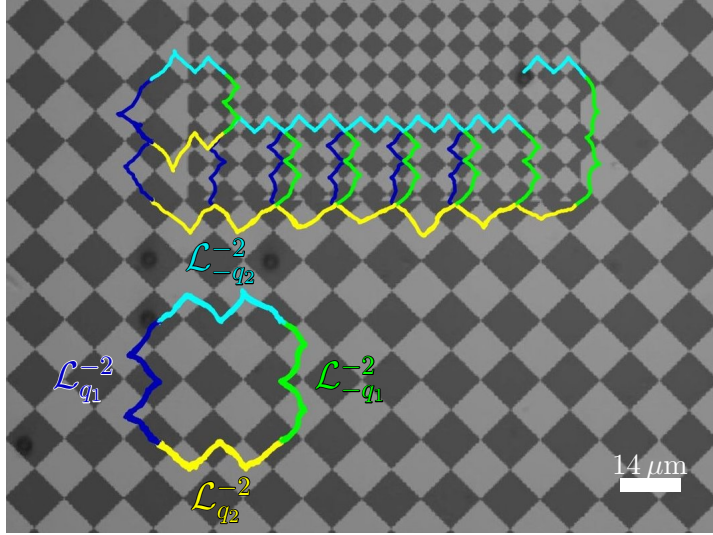


Figure 6.3: Experimental even ($n=2$) cyclotron loop on the edge; the particle is experiencing a net transport to the left because it is displaced by one large unit cell after every modulation loop. In the bulk there is no net movement. We used the loop $\mathcal{L}_{-q_2}^{-2}\mathcal{L}_{-q_1}^{-2}\mathcal{L}_{q_2}^{-2}\mathcal{L}_{q_1}^{-2}$ which runs in an inversed order than in Figure 6.2, so the resulting transport is in the opposite direction (note the rotated pattern). For better visibility a pattern image is overlaid to the microscopy image.

for even n , if the particle movement for parts of the loop meant to transport parallel to the edge behave like being in bulk and the edge is actually penetrated. The whole process is adiabatic, i.e. time reversible and running the loop backwards afterwards undoes the net movement.

If our loop instead winds around all four fence points, that means the transport from the small to the large lattice might be a ratchet, the transport distance s could be increased or decreased by one unit cell for some combinations of loops and patterns. Details when this is the case can be derived from the results discussed in section 6.5. An example of an even cyclotron loop in experiment can be seen in Figure 6.3. The bottom edge of the small pattern which is mainly crossed in the experiments has parameters similar to $\Delta x_{1\mathcal{A}}^{(s)} = 0.075a$, $\Delta x_{2\mathcal{A}}^{(s)} = 0.15a$ and $\Delta x_{2\mathcal{A}}^{(l)} = 0.5a$.

Now the question arises, what happens if n is odd? In the large unit cells the particle can only be displaced by integer multiples of a . We again look at the different parts of the modulation, see Figure 6.4. In the first part $\mathcal{L}_{-q_1}^{-3}$ ■ we cross the edge adiabatically from the large to the small lattice. Next we move n small unit cells parallel to the edge ($\mathcal{L}_{-q_2}^{-3}$ ■). Until now nothing special has happened. In the third part $\mathcal{L}_{-q_1}^3$ ■ we move back to the large lattice. If n was even there was no problem because we would observe the time inverse of the first part. For odd n we are facing a ratchet resulting the particle to go to one of the large unit cells depending on the shape of the fundamental loop where the ratchet occurs and of the pattern (and the particle height above the

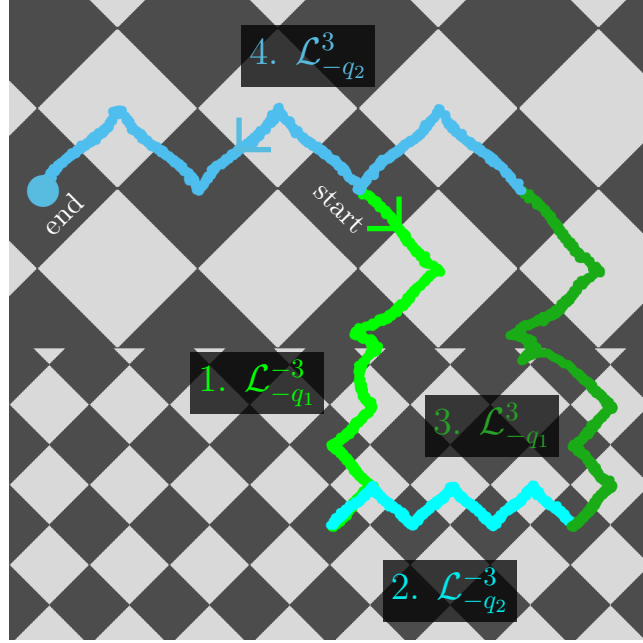


Figure 6.4: Odd ($n = 3$) cyclotron loop $\mathcal{L}_{-q_1}^{-3} \mathcal{L}_{-q_2}^{-3} \mathcal{L}_{-q_1}^3 \mathcal{L}_{-q_2}^3$ on a P_2 four-fold edge pattern using two fence points, trajectory from simulations. The particle has moved by two large unit cells after one full modulation.

pattern). Depending on the pattern we result in the cell reached by running the third part $\mathcal{L}_{-q_1}^3$ ■ starting one small unit cell to the left or to the right of the actual position. These two adiabatic paths are protecting the ratchet from going elsewhere. The fourth part $\mathcal{L}_{-q_2}^3$ ■ is again simple, moving n large unit cells parallel to the edge. The resulting edge transport for one full modulation is

$$s(n) = \pm \frac{n \pm 1}{2} \cdot a \quad (6.2)$$

for odd n if the same conditions as for even n are met. To determine the exact edge transport the results discussed in section 6.5 are needed.

6.2 Asymmetric palindrome cyclotron loops

We can now extend our cyclotron modulation loop by its time inverse. That gives us a palindrome loop like $\mathcal{L}_{q_1}^n \mathcal{L}_{q_2}^n \mathcal{L}_{q_1}^{-n} \mathcal{L}_{q_2}^{-n} \mathcal{L}_{q_2}^n \mathcal{L}_{q_1}^n \mathcal{L}_{q_2}^{-n} \mathcal{L}_{q_1}^{-n}$. We again start on the large lattice. For even n this is purely adiabatic as we have shown before and we expect no edge transport. To see this step-by-step, we can cancel out time reversed pairs next to each other without changing the resulting transport. We start with the pair in the middle ($\mathcal{L}_{q_2}^{-n} \mathcal{L}_{q_2}^n$) and continue until we have nothing left. That means we have no edge transport for even n . An example can be seen in Figure 6.5. Again the case for odd n is more complicated.

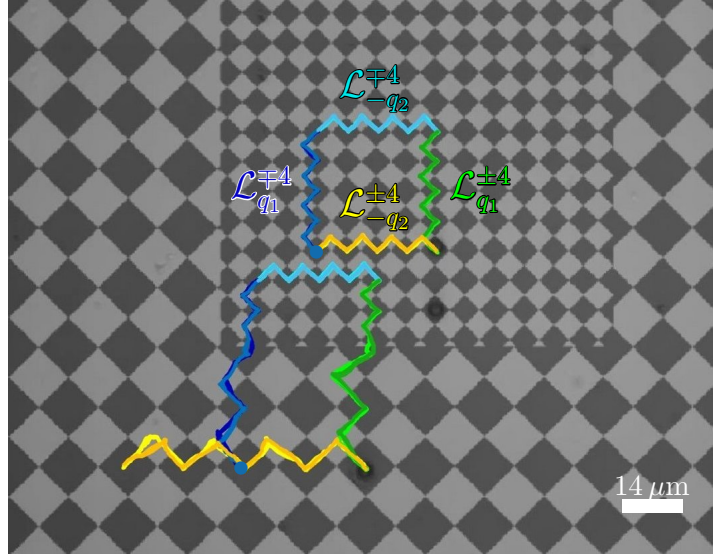


Figure 6.5: Experimental even ($n=4$) asymmetric palindrome loop $\mathcal{L}_{q_1}^{-4}\mathcal{L}_{-q_2}^{-4}\mathcal{L}_{q_1}^4\mathcal{L}_{-q_2}^4$
 $\mathcal{L}_{-q_2}^{-4}\mathcal{L}_{q_1}^{-4}\mathcal{L}_{-q_2}^4\mathcal{L}_{q_1}^4$ in bulk and penetrating the edge. There is no net transport in both cases because we have only adiabatic transport in the first half of the loop which is reversed by the second half. The loop specifiers in the image specify the forward and backward loop, the forward loop is run in a mathematical sense given by the top sign, the backwards loop by the bottom one. The start/end point is drawn as a blue circle. For better visibility a pattern image is overlaid to the microscopy image.

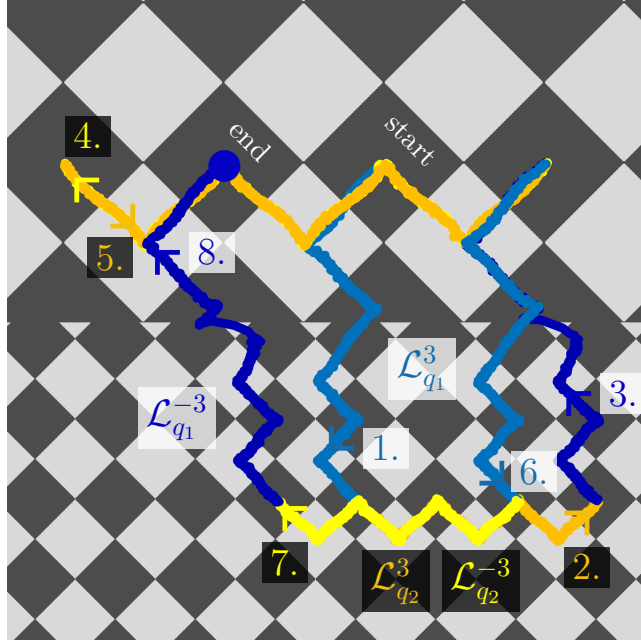


Figure 6.6: Asymmetric palindrome loop $\mathcal{L}_{q_1}^3 \mathcal{L}_{q_2}^3 \mathcal{L}_{q_1}^{-3} \mathcal{L}_{q_2}^{-3} \mathcal{L}_{q_1}^3 \mathcal{L}_{q_2}^3 \mathcal{L}_{q_1}^{-3} \mathcal{L}_{q_2}^{-3}$ run in simulation. Same colors mean identical modulation subloops in control space. The arrows on the trajectories and the corresponding numbers show the direction and order of the particle trajectories.

We will explain the odd case with the help of Figure 6.6 for $n = 3$. Looking at the middle of the loop we can cancel the pair $\mathcal{L}_{q_2}^{-3}$ (4. & 5.) because it is adiabatic motion parallel to the edge. The next pair cannot be canceled because $\mathcal{L}_{q_1}^{-3}$ (3.) is a ratchet. This ratchet occurs when transitioning from the small to the large lattice. When returning from the large to the small lattice with $\mathcal{L}_{q_1}^3$ (6.), the motion is adiabatic again and we end up one small unit cell displaced. We can describe the movement along the edge because of the ratchet as $s = \pm \frac{a}{2}$. Remembering this displacement we can now omit the pair $\mathcal{L}_{q_1}^{-3}$ (3. & 6.) and can further cancel the adiabatic pair $\mathcal{L}_{q_2}^3$ (2. & 7.). What is left is $\mathcal{L}_{q_1}^3 (\pm \frac{a}{2}) \mathcal{L}_{q_1}^{-3}$. The displacement is explicitly written down because it means that $\mathcal{L}_{q_1}^{-3}$ will contain a ratchet. This ratchet is the same as before and it results in the same displacement $\pm \frac{a}{2}$. So for odd n we can say that

$$s(n) = \pm a \quad (6.3)$$

if we start in the large lattice and the same conditions as before are fulfilled. This can be confirmed by simulations and experiments, see Figure 6.10 and Figure 6.7.

So far we have only used palindrome loops with two fence points on the four-fold edge pattern each. We would get equivalent results by swapping one or both with their opposite fence points or by changing the encircling direction. Below we want to discuss modulations using at least the fence points \mathbf{q}_1 and $-\mathbf{q}_1$. We can use these for loops with two different edge crossings.

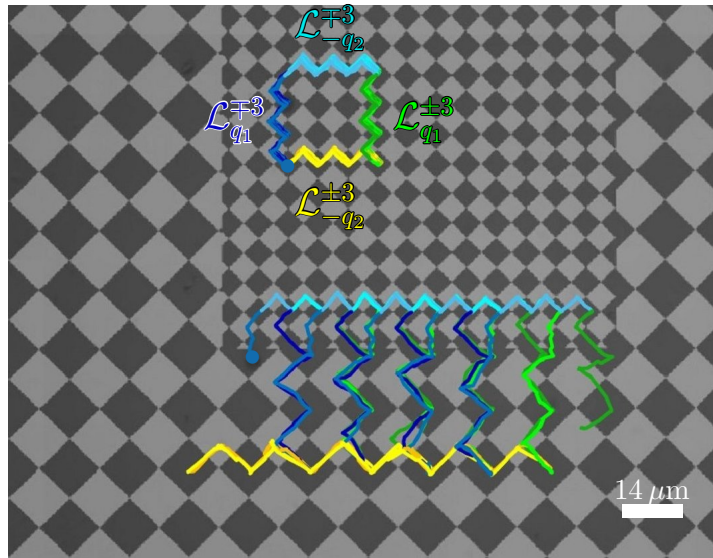


Figure 6.7: Experimental odd ($n=3$) asymmetric palindrome loop $\mathcal{L}_{q_1}^{-3}\mathcal{L}_{-q_2}^{-3}\mathcal{L}_{q_1}^3\mathcal{L}_{-q_2}^3$
 $\mathcal{L}_{-q_2}^{-3}\mathcal{L}_{q_1}^{-3}\mathcal{L}_{-q_2}^3\mathcal{L}_{q_1}^3$ in bulk and penetrating the edge. There is transport of one large unit cell every full loop penetrating the edge. For better visibility a pattern image is overlaid to the microscopy image.

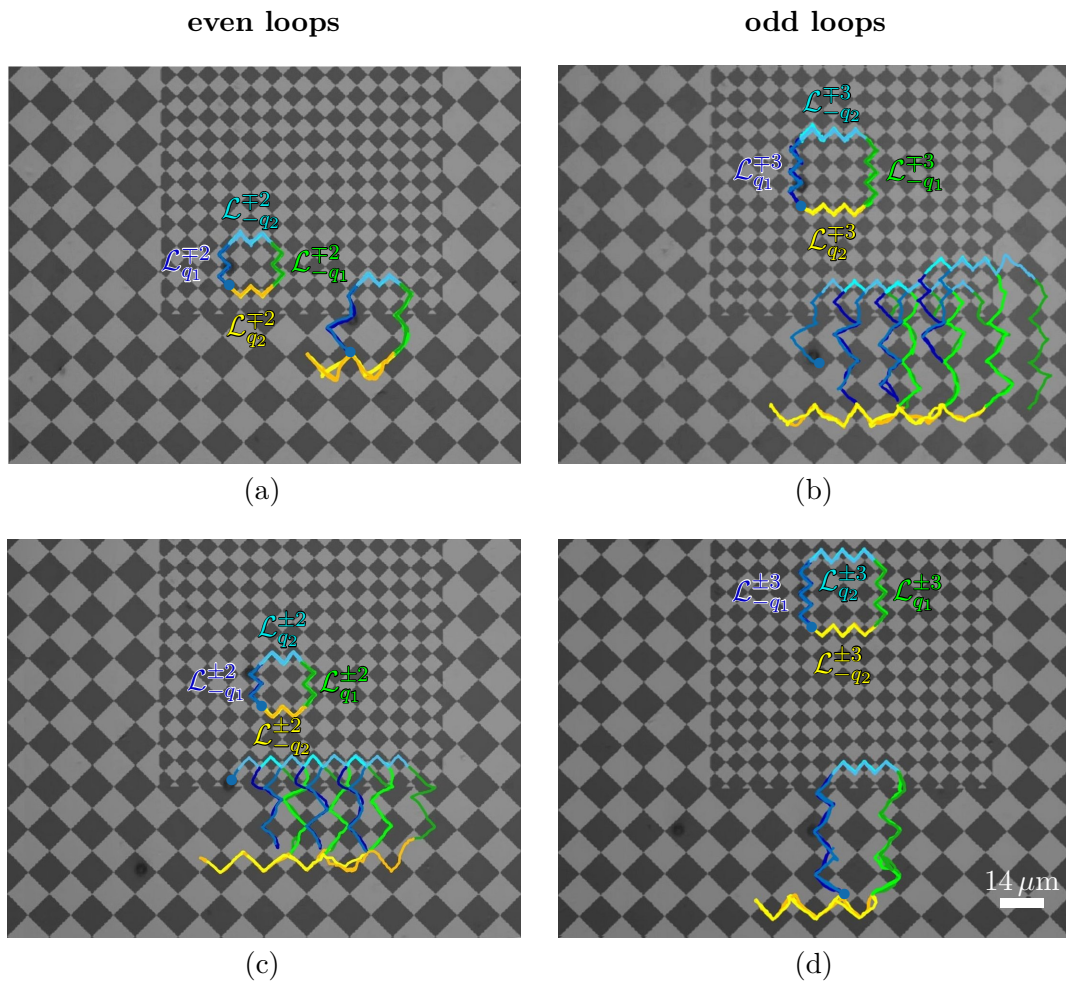

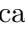

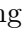
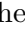
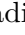
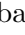
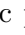


Figure 6.8: Experimental even ($n = 2$, (a) and (c)) and odd ($n = 3$, (b) and (d)) symmetric palindrome loops in bulk and penetrating the edge. Images on the top start on areas with negative (black) magnetization, images on the bottom start on areas with positive (white) magnetization. Loops starting on black areas start in the south of \mathcal{C} and in the north if starting on white. This is used to “create” a second pattern type. There is edge transport for the even loops if starting on black and for odd loops if starting on white. This is not the general case because it depends on the pattern. For better visibility the pattern image is overlaid to the microscopy images.

6.3 Symmetric palindrome cyclotron loops

First we define our new palindrome loop $\mathcal{L}_{q_1}^{-n} \mathcal{L}_{-q_2}^{-n} \mathcal{L}_{-q_1}^{-n} \mathcal{L}_{q_2}^{-n} \mathcal{L}_{q_2}^n \mathcal{L}_{-q_1}^n \mathcal{L}_{-q_2}^n \mathcal{L}_{q_1}^n$. The loop has a symmetry plane perpendicular to the edge in control space. Therefore we call such loops symmetric loops. Examples from the experiments are given in Figure 6.8. We start again by canceling the adiabatic pair $\mathcal{L}_{q_2}^{-n}$  $\mathcal{L}_{q_2}^n$ . The next pair $\mathcal{L}_{-q_1}^{-n}$  $\mathcal{L}_{-q_1}^n$  may contain a ratchet or not. We cannot determine this, because we do not have any other edge transition winding around $-q_1$. So we remember this pair with $s = 0, \pm \frac{a}{2}$. The next adiabatic pair $\mathcal{L}_{-q_2}^{-n}$  $\mathcal{L}_{-q_2}^n$  cancels and we remain with $\mathcal{L}_{q_1}^{-n}$  $(0, \pm \frac{a}{2}) \mathcal{L}_{q_1}^n$ . For a general edge pattern the two edge crossing fundamental loop pairs are not correlated to each other so we can again say that $s = 0, \pm \frac{a}{2}$. Adding the two single results together in any combination we get

$$s(n) = 0, \pm a \quad (6.4)$$

if winding around $\pm q_2$ is always adiabatic and we have actually crossed the edge. For patterns having a common symmetry plane perpendicular to the edge, the edge crossing parts are now correlated and the displacement at the two different ratchets cancels each other or we don't have ratchets at all, so $s = 0$ in these cases.

If we build palindrome loops reversing on the small lattice, we observe no edge transport at all if our first edge crossing is adiabatic. The path entering the small lattice is always adiabatic, so reversing this path also leads to an adiabatic path back to the large lattice. If the first edge crossing is not adiabatic, we observe a one-time transport for the first run of the loop. After that the particle is offset one small unit cell and the next loop will be purely adiabatic.

We have seen that the edge transport depends on the type of pattern, so we will try to classify them. Symmetrical patterns can be divided into two types, one where we have a symmetry plane passing only black areas and one type with a symmetry plane passing only white areas. We call these non-alternating mirror planes. As we start on black in the large lattice, our start and end points lie on non-alternating mirror planes for some symmetric patterns and on alternating mirror planes for other symmetric patterns. If the movement of the particle in the small lattice parallel to the edge is mirror symmetric to the non-alternating plane when running a symmetric palindrome loop, we expect no ratchet, because the adiabatic movement from the small to the large lattice is mirrored. Otherwise we expect to see two ratchets, both when crossing the edge from the small to the large lattice, see Figure 6.9.

Non symmetrical pattern types are not that easy to describe and the movement depends on the exact shape of the loop and the particle height above the pattern. We have simulated many different patterns for a particle height $z = 0.2a$ with different loops to get an idea of the different possible particle behaviors. The methodology used has already been described in chapter "Simulations and loop generation". For every pattern we run different loops and record the position differences between start and end, the edge transport. These can be represented in phase diagrams. As we have at least four¹

¹An additional parameter would be the height z above the pattern

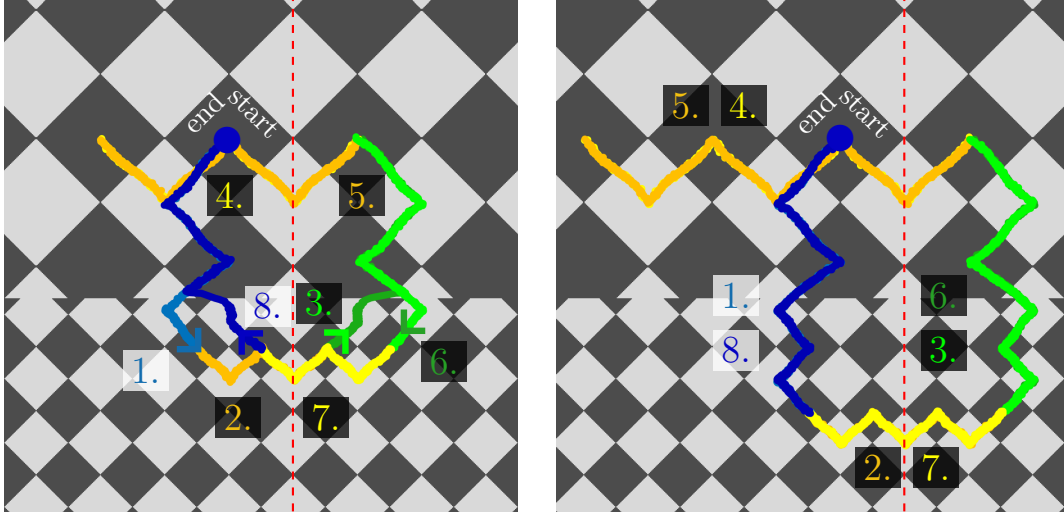


Figure 6.9: Symmetric palindrome loop $\mathcal{L}_{q_1}^n \mathcal{L}_{q_2}^n \mathcal{L}_{-q_1}^n \mathcal{L}_{q_2}^{-n} \mathcal{L}_{q_1}^{-n} \mathcal{L}_{q_2}^{-n} \mathcal{L}_{-q_1}^{-n} \mathcal{L}_{q_2}^{-n} \mathcal{L}_{q_1}^{-n}$ on a symmetric pattern starting on an alternating mirror plane, trajectories from simulations. The numbers give the succession of the trajectories for the different subloops and the arrows the direction in case of hysteresis. On the left, a loop with even $n = 2$ is shown. Because the movement in the small pattern parallel to the edge (2. or 7.) has no common non-alternating mirror plane (dashed red) with the pattern, we see ratchets and thus hysteresis. The right image shows the loop for odd $n = 3$. Here we see the common non-alternating symmetry plane and the motion is purely adiabatic. In both cases there is no net edge transport.

parameters (three for the pattern and $\Delta\phi$), we can not show all results in one diagram. Instead we plot diagrams for fixed $\Delta x_{1\mathcal{A}}^{(s)}$ and $\Delta\phi$ showing a $\Delta x_{2\mathcal{A}}^{(s)} - \Delta x_{2\mathcal{A}}^{(l)}$ -plane.

6.4 Phasediagrams for palindrome loops

Using the phase diagrams, we first confirm the statements for the non-symmetric loops. We look at phase diagrams for odd and for even loops. Even loops show no transport at all as expected, the phasediagram contains only black (no transport) and white (no edge crossing) regions. The results for the odd asymmetric palindrome loops, examples are given in Figure 6.10, confirm the expectations for all patterns where the particle can successfully cross the edge in both directions for the given $\Delta\phi$. We can see phases of edge transport parallel and anti-parallel to \mathbf{a}_1 . There is no obvious rule how the transport direction depends on the parameters. Near the transition between phases we see different directions originating from randomized edge crossings, influenced by the random forces. At white areas no proper transport across the edge from the large to the small pattern could be achieved with the loop used.

Looking at the results for the symmetric loops in Figure 6.11, we can see phases

with no edge transport and with edge transport of $\pm a$ as expected. For symmetrical patterns we see that no net transport occurs. Looking at the patterns with $\Delta x_{1\mathcal{A}}^{(s)} = \frac{1}{8}a$ and $\Delta x_{1\mathcal{A}}^{(s)} = \frac{3}{8}a$ which are mirror images of each other, we see that the shape of the phasediagram is identical, only the color (edge transport direction) is different. This is obvious, because the loop itself is symmetrical, so mirroring just the pattern equals mirroring the whole system, including the resulting edge current.

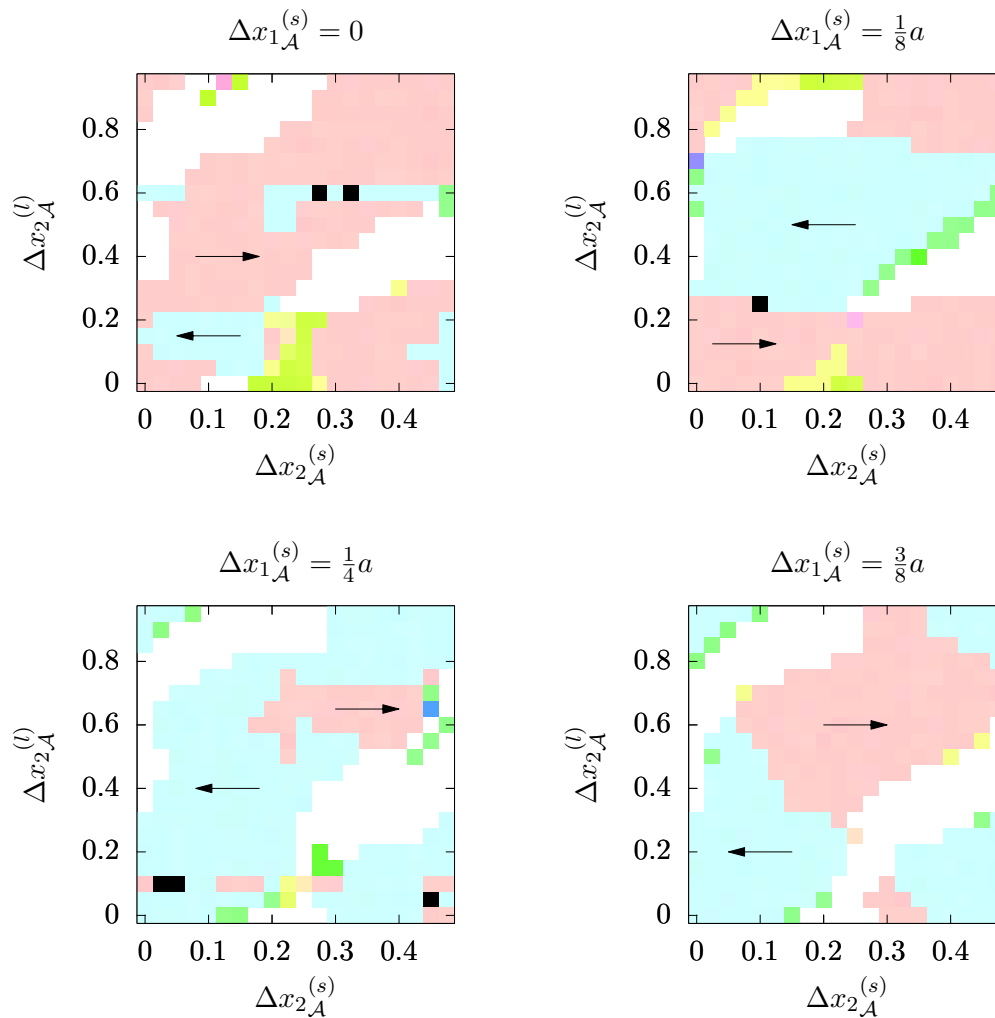


Figure 6.10: Phasediagrams for $\Delta\phi = 35^\circ$, asymmetric odd palindrome loops winding around $-q_1$ for movement perpendicular to the edge; red phases are transporting particles one unit cell a to the right for the given loop, blue phases to the left, other colors are caused by particles unable to cross the edge properly.

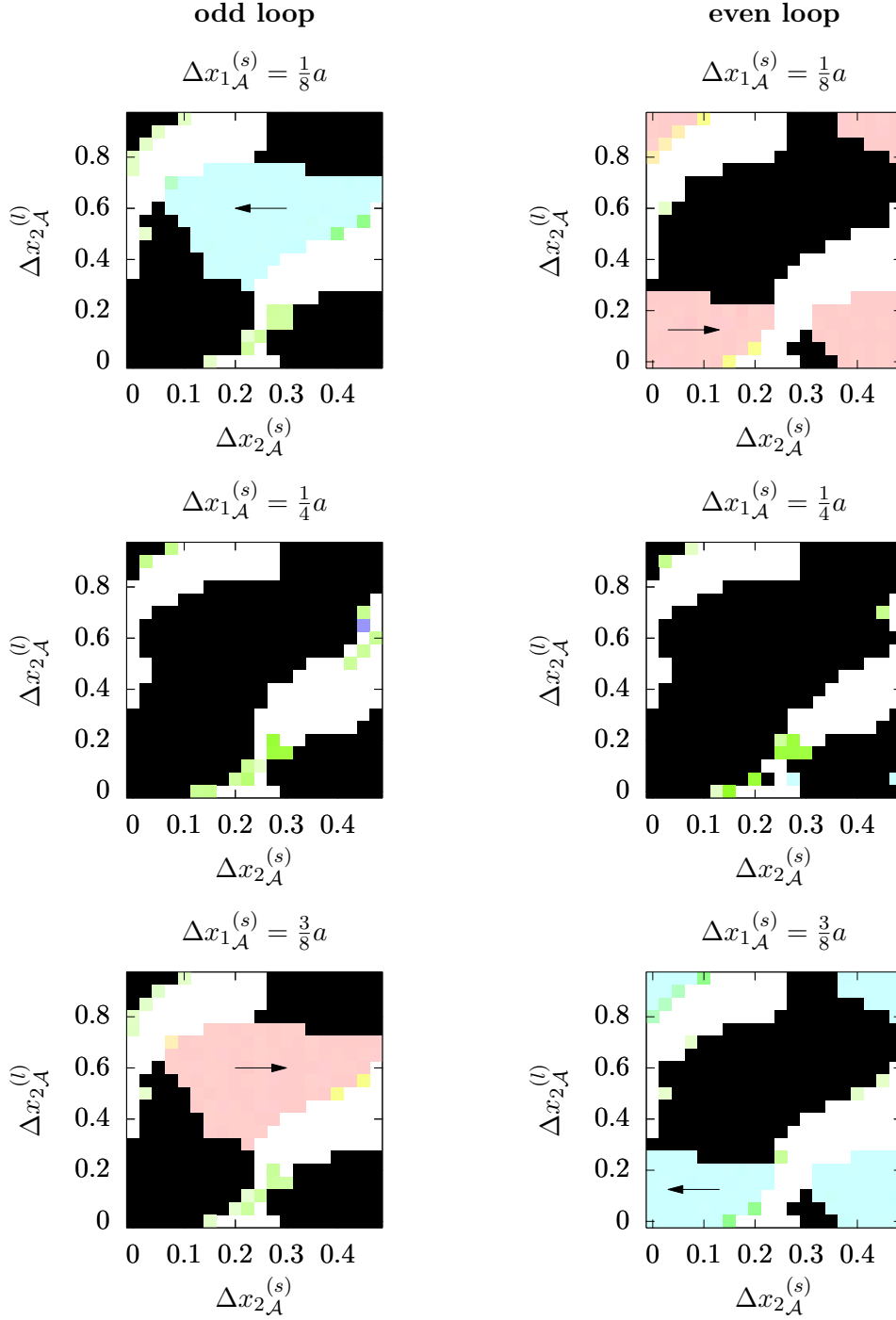


Figure 6.11: Phasediagrams for $\Delta\phi = 35^\circ$, symmetric palindrome loops, left odd loops, right even loops, colors are the same as in Figure 6.10. The symmetric patterns ($\Delta x_{1\mathcal{A}}^{(s)} = \frac{1}{4}a$) show no transport (black) as expected. For a given pattern there is transport either for odd or even symmetric palindrome loops or no transport at all, also depending on $\Delta\phi$.

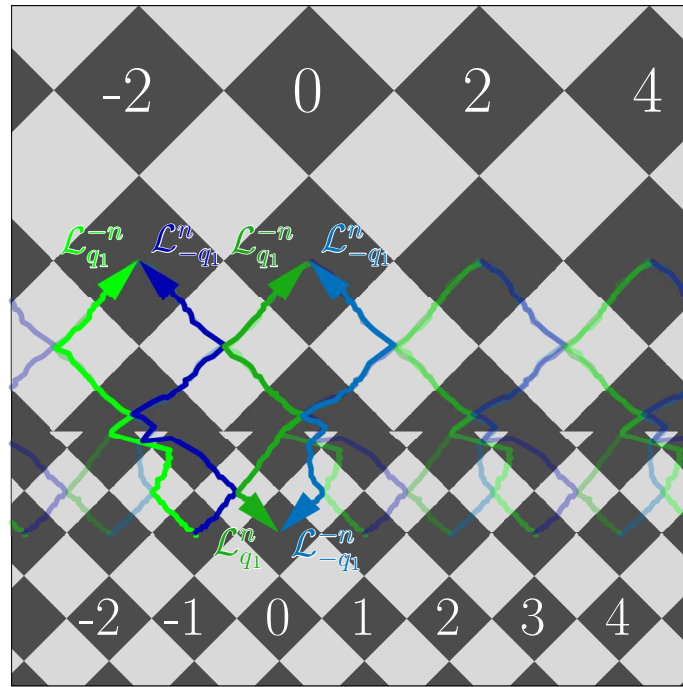


Figure 6.12: Example of deriving behavioral modes from particle trajectories for an α_2 mode. The numbers are relative coordinates in x_1 -direction. Trajectories with two arrows are adiabatic, the others show ratchets. The result is translation invariant along the edge, so adding $2n$ ($n \in \mathbb{Z}$) to every coordinate number gives us the same result, drawn as transparent trajectories. The loops used are $\mathcal{L}_{\pm q_1}^{\pm 2}$. The labels at the arrow tips indicate the used modulation for the trajectory.

6.5 Behavioral modes

The phase diagrams for the different loops show only part of the possible edge crossings each, so it makes sense to combine them. We define phases containing all the information on the edge transport for all previous cyclotron and cyclotron palindrome loops. These transport modes describe the behavior for a certain $\Delta\phi$ and pattern, thus we will call them behavioral modes.

For a given pattern $P_2(\Delta x_{1\mathcal{A}}^{(s)}, \Delta x_{2\mathcal{A}}^{(s)}, \Delta x_{2\mathcal{A}}^{(l)})$ we start in the small or large lattice on a black area and wind around \mathbf{q}_1 and $-\mathbf{q}_1$ using fundamental loops $\mathcal{L}_{\pm q_1}^{\pm n}[\Delta\phi]$ with a fixed $\Delta\phi$ in the right mathematical sense for crossing the edge in any of the six distinct ways. The system is translation invariant along the edge, so we have to simulate only these six trajectories to get all the information we need to define our behavioral modes. We place the origin of the x_1 coordinate within a black square of the large lattice and use a second origin of the x_1 coordinate in the small lattice such that edge crossing path induced by $\mathcal{L}_{q_1}^n$ connects the two origins. With this choice of coordinates, the movement across the fence in \mathbf{a}_1 direction is zero for the modulation $\mathcal{L}_{q_1}^n$. Furthermore we specify the x_1 coordinate in units of the size of a unit cell of the small pattern. We note down the resulting coordinate parallel to the edge for the other modulation $\mathcal{L}_{-q_1}^{-n}$ which also transfers a colloid from the large to the small lattice. The two inverse loops $\mathcal{L}_{q_1}^{-n}$ and $\mathcal{L}_{-q_1}^n$ transfer a colloidal particle in opposite direction, i.e. from the small towards the large lattice. For this transfer there are two possible distinct starting points $x_1 = 0$ and $x_1 = -1$. Thus, we have two transfers from the large to the small lattice and four transfers from the small towards the large lattice. An example is given in Figure 6.12. We call a unique combination of the resulting particle coordinates in the small and large lattice after crossing the edge a behavioral mode. Any of these combinations we found are listed in Table 6.1.

By extending this data using its periodicity for other starting cells, one can see symmetries in the behavioral modes. We extend the coordinates resulting of the transfer from the small towards the large lattice. We take α_1 as an example where we read the small \rightarrow large columns as $(0, 0, \bar{0}, \bar{0})$ for starting at the small cell coordinates $x_1 = -1$ and $x_1 = 0$ which is overlined to indicate the start position at the coordinate origin. We extend these values for starting in the small cell at $x_1 = 1$. Because of the periodicity of two small unit cells in x_1 direction, we take the values for the starting cell $x_1 = -1$, add two, and assign them to the starting cell at $x_1 = 1$. Our resulting coordinates in the large lattice are now $(0, 0, \bar{0}, \bar{0}, 2, 2)$. We now want to mirror the coordinates for the transfer from the small to the large pattern as well as the loops at a mirror plane perpendicular to the edge. This equals mirroring the pattern at the same plane. Mirroring the loops is easy, because we only have to swap $\mathcal{L}_{-q_1}^n$ with $\mathcal{L}_{q_1}^{-n}$. For mirroring the coordinates in the small lattice we have to find the x_1 -position of the mirror plane in the coordinate system of the small lattice. Looking at the columns for the large \rightarrow small transition we find that both are zero for the mode α_1 . They give us the position of the mirror plane in the small lattice which is at $x_1 = 0$ in this case. In general the mirror plane is at the mean value of the two entries. To perform the mirror operation for the starting coordinates in the small lattice we mirror them at this mirror plane position, i.e. reverse




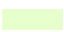
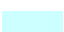




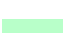
Name	Color	large \rightarrow small		small \rightarrow large			
		$L_0, \mathcal{L}_{q_1}^n$	$L_0, \mathcal{L}_{-q_1}^{-n}$	$S_{-1}, \mathcal{L}_{-q_1}^n$	$S_{-1}, \mathcal{L}_{q_1}^{-n}$	$S_0, \mathcal{L}_{-q_1}^n$	$S_0, \mathcal{L}_{q_1}^{-n}$
α_1		0	0	<u>0</u>	<u>0</u>	0	0
α'_1		0	1	-2	<u>0</u>	<u>0</u>	0
α_2		0	0	<u>-2</u>	<u>-2</u>	0	0
α'_2		0	1	-2	<u>-2</u>	<u>-2</u>	0
β_1		0	0	<u>-2</u>	<u>0</u>	0	0
β'_1		0	1	-2	<u>-2</u>	<u>0</u>	0
β_2		0	0	<u>0</u>	<u>-2</u>	0	0
β'_2		0	1	-2	<u>0</u>	<u>-2</u>	0
β_3		0	2	<u>-2</u>	<u>-2</u>	-2	0
β'_3		0	-1	0	<u>0</u>	<u>0</u>	0

Table 6.1: Behavioral modes with name and color. The table gives the coordinates in x_1 -direction for the target pattern as shown in Figure 6.12. The starting coordinate x_1 is given in the table head in the form of L_{x_1} (starting in large pattern) or S_{x_1} (starting in small pattern). The table head also specifies the modulation $\mathcal{L}_{\pm q_1}^{\pm n}$ used to cross the edge. The resulting coordinate can then be read from the table. The coordinates for the large pattern are given in multiples of two. Underlined numbers indicate a ratchet. The phase pairs α_1/α_2 and α'_1/α'_2 are mirror symmetric to each other, β -phases are self symmetric. Phases marked with a prime have white and black exchanged on the pattern.

their order keeping the markings for $x_1 = 0$ at the same place relative to the mirror plane. We then mirror the resulting coordinates in the large lattice at the mirror plane there, which is always at $x_1 = 0$, so we change the sign of the coordinates resulting in the large lattice. For our α_1 mode we get $(-2, -2, \bar{0}, \bar{0}, 0, 0)$ after performing both steps. The resulting x_1 coordinates for the large \rightarrow small transition do not change when performing the mirror operation. So as a result we have table entries for large \rightarrow small $(0, 0)$ and for small \rightarrow large $(-2, -2, \bar{0}, \bar{0})$. If we compare these with Table 6.1 we note that these are identical to the behavioral mode α_2 . We can conclude that α_2 is the mirror image of α_1 . Such non self symmetric (asymmetric) modes are marked with α and have a symmetry partner each. Asymmetric mode pairs symmetric to each other are α_1/α_2 and α'_1/α'_2 . If we repeat the mirror operation on a different type of mode, for example on β_1 , the resulting coordinates are the same, so the mode is invariant under this operation. We call such modes self symmetric modes and mark them with β .

Phases for patterns sharing the same fences because black and white areas are exchanged are marked with the same letter and number such as α_1 , but the ones behaving like having common non-alternating symmetry planes through white areas when using symmetric palindrome loops get a prime (α'_1).

In the phase diagrams we give a color to each mode. A list of the different phases with

Mode	even		odd	
	symmetric	symmetric	asymmetric q_1	asymmetric $-q_1$
α_1 ■	○	→	→	→
α'_1 ■	→	○	→	→
α_2 ■	○	←	←	←
α'_2 ■	←	○	←	←
β_1 ■	○	⊖	→	←
β'_1 ■	⊖	○	←	→
β_2 ■	○	⊖	←	→
β'_2 ■	⊖	○	→	←
β_3 ■	○	⊖	←	→
β'_3 ■	⊖	○	→	←

Table 6.2: Palindrome cyclotron loop edge transport directions for different behavioral modes and different palindrome cyclotron loops. The loops are specified by their type and the winding point if necessary. The directions are given for patterns with large lattice constant on top, small on bottom. The symbol ○ indicates no net movement without hysteresis, the symbol ⊖ with ratchets and thus hysteresis.

their color is given in Table 6.1. The colors of modes symmetric to each other have the same hue but a different saturation. Modes that are detected only a few times, mostly occurring at transitions between bigger phases, are colored in black and are not further discussed. For patterns at unpainted areas the particle cannot cross the edge for one loop type, usually when trying to move from the large into the small lattice. We have computed phase diagrams for $\Delta\phi = 35^\circ$ and 70° shown in Figure 6.13 and Figure 6.14.

If we slightly move away from symmetric or maximal non-symmetric patterns by changing $\Delta x_{1,\mathcal{A}}^{(s)}$ by a small amount, we observe that either the phase diagram for small or for big $\Delta\phi$ changes quickly. For small $\Delta\phi$ the asymmetric phases get predominant, for large $\Delta\phi$ symmetric phases. One could say modulation loops with small $\Delta\phi$ are less “symmetric” than modulation loops with large $\Delta\phi$. An example for the fast transition from maximal non-symmetric patterns is shown in Figure 6.15.

Drawing visual representations of the different asymmetric behavioral modes, such as in Figure 6.12, we can easily see which phase has edge transport for which loop. For the symmetric palindrome loops where we had $s(n) = 0, \pm a$, we can now give detailed information about direction and existence of edge transport for the different phases, as well as the direction for the asymmetric palindrome loops. They are summarized in Table 6.2.

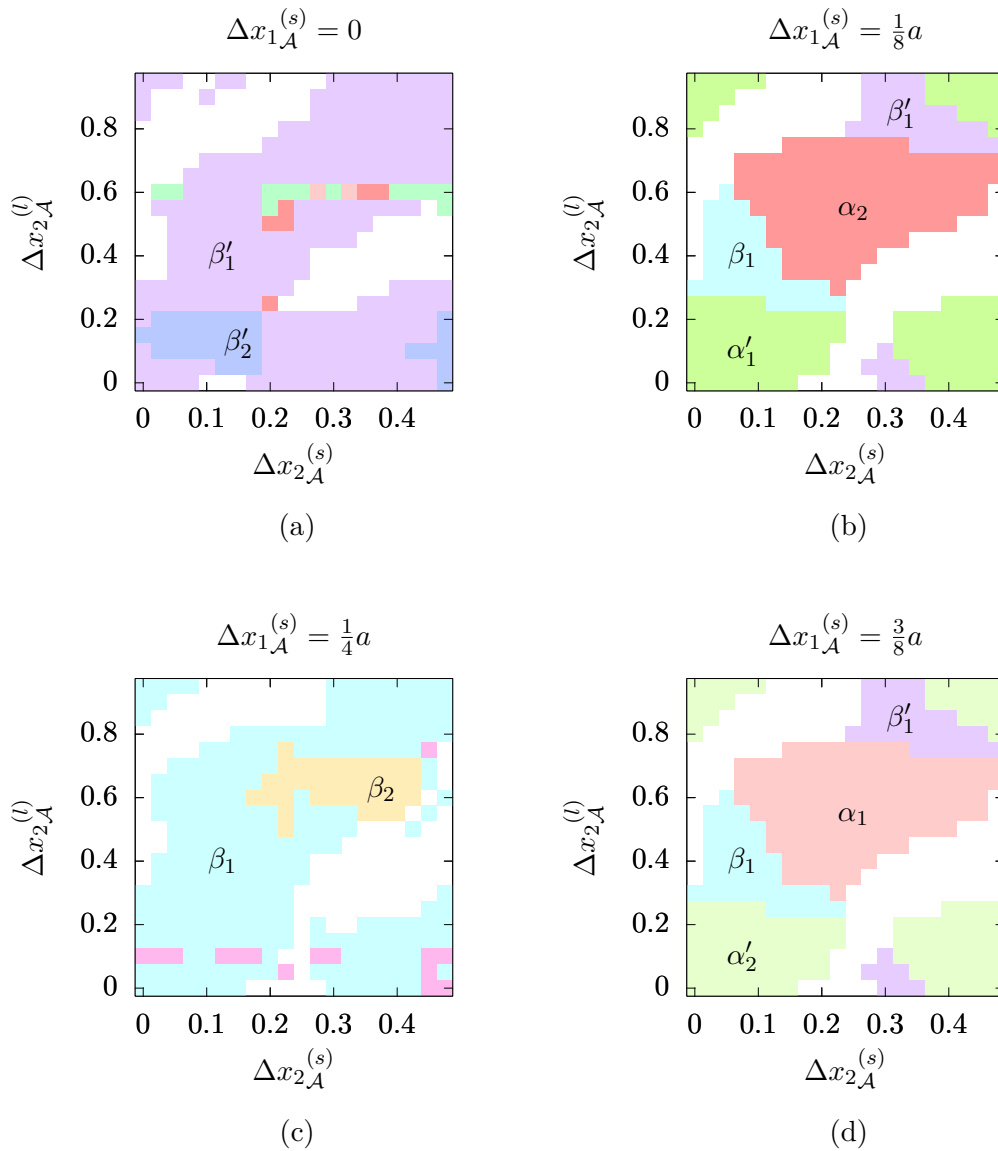
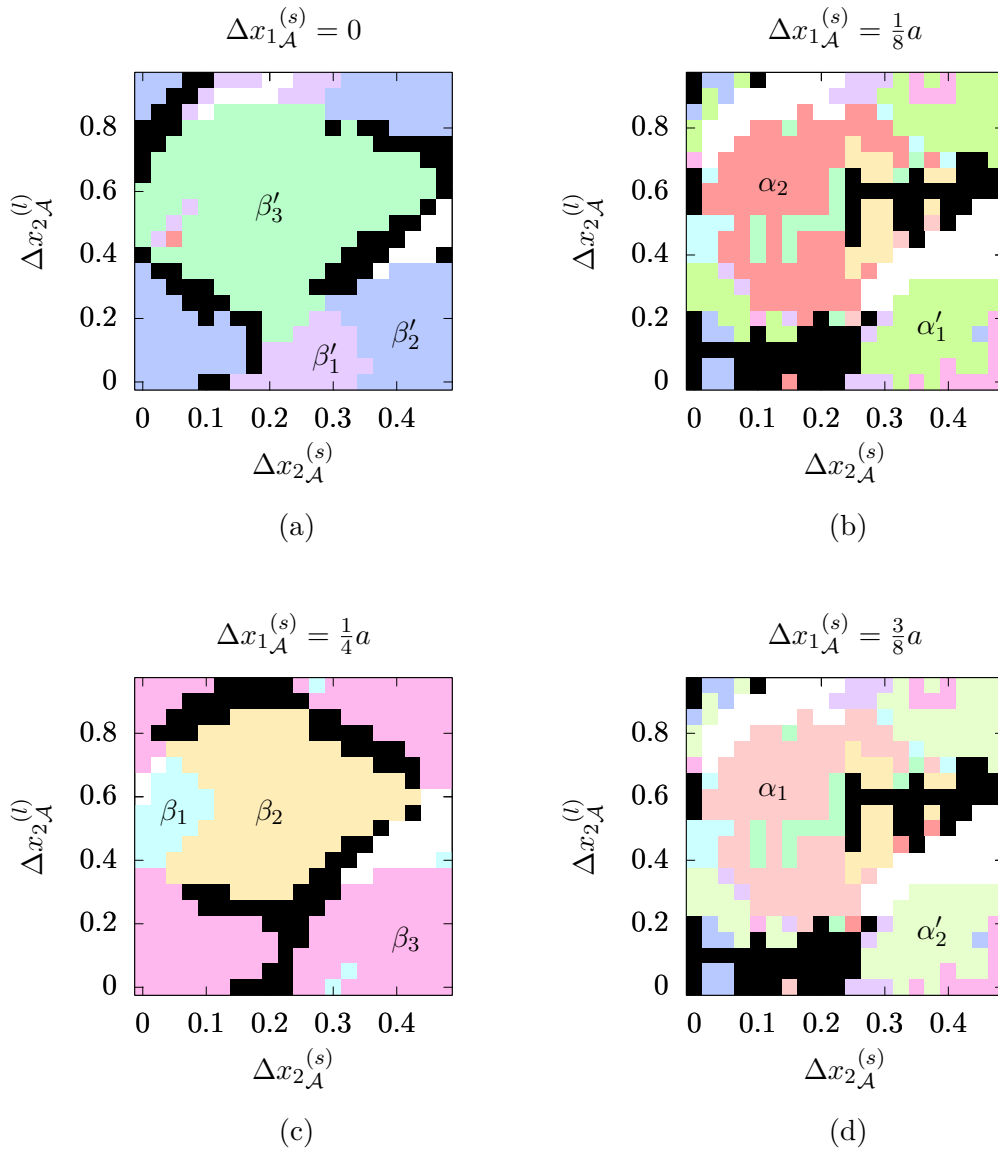


Figure 6.13: Phas diagrams showing behavioral modes for $\Delta\phi = 35^\circ$. $\Delta x_{1A}^{(s)}$ are chosen such that we get symmetric ((a) and (c)) and maximal non-symmetric patterns ((b) and (d)).

Figure 6.14: Phasediagrams showing behavioral modes for $\Delta\phi = 70^\circ$.

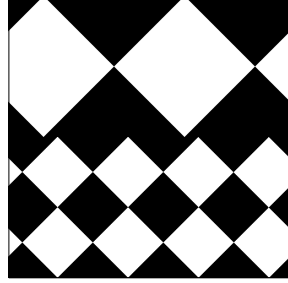
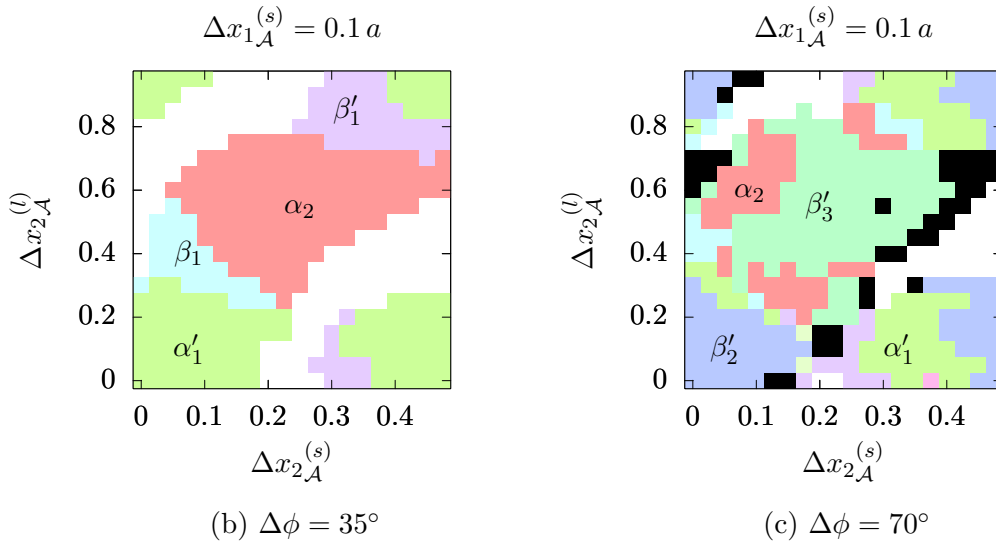
(a) $\Delta x_{1, \mathcal{A}}^{(s)} = 0.1 a$ 

Figure 6.15: Phasediagrams for $\Delta\phi = 35^\circ$ and 70° ((b) and (c)) where $\Delta x_{1, \mathcal{A}}^{(s)} = 0.1 a$ is chosen close to $\Delta x_{1, \mathcal{A}}^{(s)} = \frac{1}{8}a = 0.125 a$, which are maximal non-symmetric patterns. The resulting phase diagram for $\Delta\phi = 35^\circ$ is very close to the phase diagram for $\Delta x_{1, \mathcal{A}}^{(s)} = \frac{1}{8}a$ (Figure 6.13b). The phase diagram for $\Delta\phi = 70^\circ$ instead is similar to the phase diagram for $\Delta x_{1, \mathcal{A}}^{(s)} = 0$ (Figure 6.14a) and has predominantly symmetric phases although the patterns are still asymmetric. An example for a pattern with $\Delta x_{1, \mathcal{A}}^{(s)} = 0.1 a$ is shown in (a).

6.6 Symmetry considerations

We now want to discuss the change of direction of edge transport $s(\mathcal{L}_{Pal}, P_2)$ for palindrome loops with fixed $\Delta\phi$ based on symmetry considerations for the pattern P_2 , the palindrome modulation loop \mathcal{L}_{Pal} and the symmetry of the corresponding behavioral mode $\alpha_i^{(l)}$ or $\beta_i^{(l)}$. We can introduce a symmetry operation σ mirroring any of them with a mirror plane perpendicular to the edge.

All of these can be mirror symmetric or can be mirrored to a distinct mirror image using the symmetry operation σ with the mirror plane perpendicular to the edge. If something is already symmetric, it is invariant under that operation, such that

$$\sigma\mathcal{L}_{Pal,sym} = \mathcal{L}_{Pal,sym} \quad (6.5a)$$

and

$$\sigma P_{2,sym} = P_{2,sym}. \quad (6.5b)$$

Starting by mirroring the pattern $P_{2,asym}$ and the loop $\mathcal{L}_{Pal,asym}$ if both are not symmetric, we have mirrored the whole system which mirrors the transport direction as well, so

$$s(\sigma\mathcal{L}_{Pal,asym}, \sigma P_{2,asym}) = -s(\mathcal{L}_{Pal,asym}, P_{2,asym}). \quad (6.6)$$

Mirroring the pattern (or the loop) if the loop (or the pattern) is symmetric mirrors the transport direction as well:

$$s(\mathcal{L}_{Pal,sym}, \sigma P_{2,asym}) = -s(\mathcal{L}_{Pal,sym}, P_{2,asym}) \quad (6.7a)$$

and

$$s(\sigma\mathcal{L}_{Pal,asym}, P_{2,sym}) = -s(\mathcal{L}_{Pal,asym}, P_{2,sym}) \quad (6.7b)$$

For the pattern and or the loop or both being symmetric, mirroring them changes nothing, obviously. If we mirror just the pattern or the loop, both being asymmetric, we can not easily say how the edge transport changes. But by using our previous mentioned behavioral modes, we can give more information about that. If we look at symmetric modes β , they are equivalent to symmetric patterns, so mirroring the loop mirrors the edge transport, mirroring the pattern does nothing. For asymmetric modes α , mirroring the loop does not change the transport direction, whereas mirroring the pattern changes it. In this case we see a behavior like we had a symmetric loop, even if the loop is asymmetric:

$$s(\sigma\mathcal{L}_{Pal,asym}, P_{2,asym}) = \begin{cases} s(\mathcal{L}_{Pal,asym}, P_{2,asym}) & \text{if in } \alpha_i^{(l)} \text{ mode} \\ -s(\mathcal{L}_{Pal,asym}, P_{2,asym}) & \text{if in } \beta_i^{(l)} \text{ mode} \end{cases} \quad (6.8a)$$

and

$$s(\mathcal{L}_{Pal,asym}, \sigma P_{2,asym}) = \begin{cases} -s(\mathcal{L}_{Pal,asym}, P_{2,asym}) & \text{if in } \alpha_i^{(l)} \text{ mode} \\ s(\mathcal{L}_{Pal,asym}, P_{2,asym}) & \text{if in } \beta_i^{(l)} \text{ mode} \end{cases} \quad (6.8b)$$

6.7 Fences

Using the method from section 5.5 we can find fences in control space from simulation results for specific patterns. They represent the location of ratchets, so they get visible only near the edge as the motion in the bulk is purely adiabatic. The fence locations for modulations with different $\Delta\phi$ for transporting the particle from the small into the large lattice are combined to get a representation of the full fence. We are only interested in patterns where the transport from the large to the small lattice is adiabatic for the majority of loops. As we don't see fences in adiabatic transport we don't regard fence diagrams for transfers from the large to the small lattice as they would be almost empty. The fundamental modulation loops $\mathcal{L}_{q_1}^{-n}$ and $\mathcal{L}_{-q_1}^n$ used to create the fence diagrams are shown in Figure 6.17. Starting with the particle at one of the two different starting points along the x_1 axis in the small lattice shows different fences, colored differently in magenta and cyan. Near the bulk fence points fences with different colors coexist, because there we can also see parts of enlarged bulk fence points. These lead to adiabatic transport if they are encircled without crossing any other fence. Trying to transport a particle from the large to the small lattice with a modulation passing through an enlarged fence point usually leads to a ratchet back to the large lattice such that no edge crossing is possible. For patterns where we observe that the particle is unable to cross the edge in both directions even with $\Delta\phi = 35^\circ$ these fence points are very large or can be unfolded and connected with a neighboring enlarged fence point.

Looking at the results, Figure 6.18 and Figure 6.19, one can clearly see bifurcation points separating the fence segments. By comparing the fences with the behavioral mode phase diagrams for different $\Delta\phi$ we can map the fence segments to behavioral modes. We observe that for each proper transport loop from the small to the large lattice there is only one ratchet involved. It can occur when the external magnetic field direction moves from the south to the north pole or the other way round. That is because we cross the edge only once during one modulation loop and bulk movements are always adiabatic. That means we see a fence only in half of the ϕ -space, the other ϕ are at the part of each loop where no ratchet occurs.

For a non-symmetric pattern the resulting fence is also not symmetric, see Figure 6.18. If we add half of their periodicity to all three parameters $\Delta x_{1\mathcal{A}}^{(s)}$, $\Delta x_{2\mathcal{A}}^{(s)}$ and $\Delta x_{2\mathcal{A}}^{(l)}$ of the pattern we get a fence diagram which looks different. Looking closer one can see similarities between the fences. If we mirror one of the two fence diagrams and shift it by $\phi = 180^\circ$ we can see the relation between them. If you look at the phase diagrams, performing this parameter shift leads to phases with an identical shape, see Figure 6.16. This is because this specific pattern parameter change equals exchanging positive and negative magnetization as described in Equation 2.4, so the relevant fence segments are the same for both patterns.

Looking at symmetric patterns, Figure 6.19, we see that the fence in control space has a symmetry plane perpendicular to the edge. Only the colors are interchanged in the mirror image if the pattern has no non-alternating mirror plane for the magnetization we start on. In this case there is only one adiabatic path for every starting cell in the small

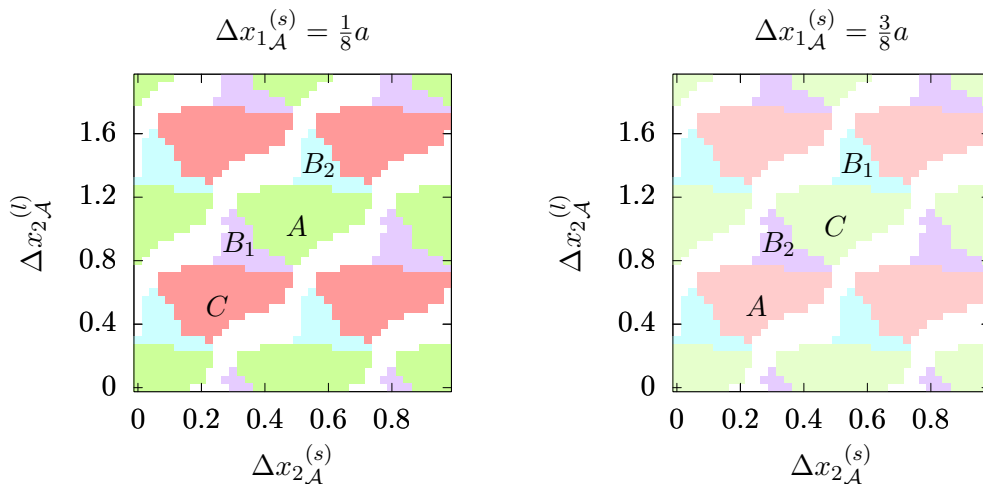


Figure 6.16: Phas diagrams for behavioral modes to show the periodicity of the phase diagrams and the similarity between related modes, marked with the same letter. Modes marked with A and C have the same shape as they are a symmetry pair, modes B are self-symmetric. Both phases marked with C (red and light green) have black and white exchanged, the same applies for patterns marked with A , B_1 and B_2 .

lattice and thus one ratchet path to the large lattice. So the other ratchet has to occur starting from another position in the small lattice, explaining the change in color.

Furthermore, the fence diagrams show that the behavioral modes discussed before can only be used for a constant $\Delta\phi$. If we want to use loops crossing the fence at different $\Delta\phi$, this simple representation of behavioral modes is not valid any more because the relative positions are based on one edge crossing result which might not be the same for different $\Delta\phi$. Going from north to south at a different $\Delta\phi$ than from south to north, we don't know which behavioral mode applies because we cannot say which fence segment we crossed without looking at the fence diagrams.

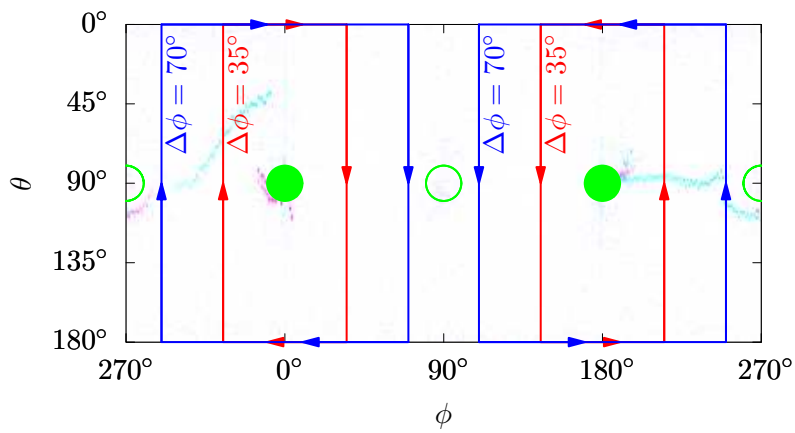


Figure 6.17: Examples for loops used to find the fences, winding around the filled green circles, showing the location of fence points for the bulk. The fence is marked in magenta and cyan for the two possible starting positions in the small pattern.

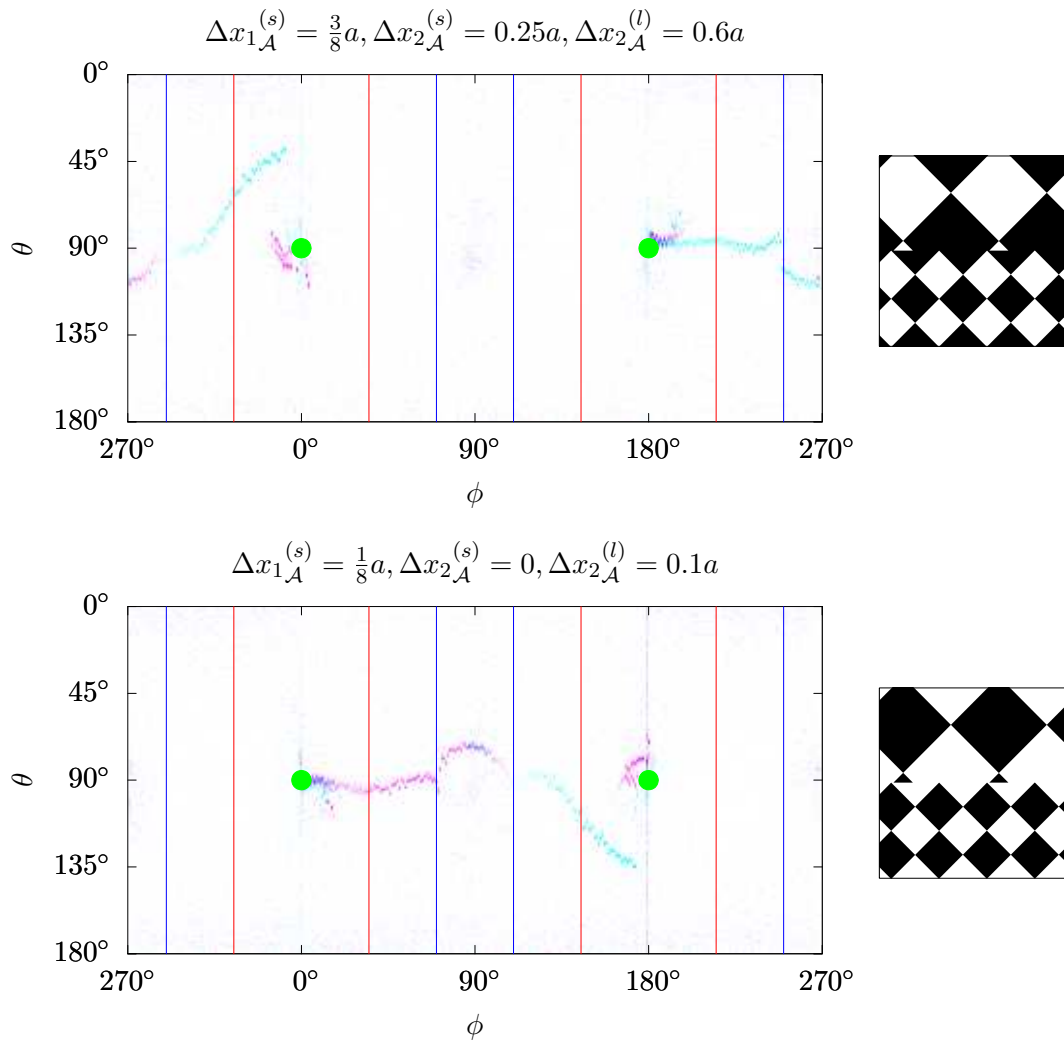


Figure 6.18: Fences for a two non-symmetric patterns, the lines indicate the loops used to create the phase diagrams. Both patterns are chosen such that only black and white are exchanged so they share the same fences, only shifted by 180° in ϕ -direction and mirrored at the equator ($\theta = 90^\circ$) and the colors have changed. For the top pattern, the red loops at 35° and 215° cross the middle of the fence segment, which equals the α_1 phase in Figure 6.13d. The blue loops at 70° and 250° directly cross bifurcation points, they are between multiple behavioral modes, visible in Figure 6.14d. In the bottom pattern the fences crossed by the red loops are responsible for phase α'_1 , the blue loops hit the bifurcation point, they are again between multiple behavioral modes.

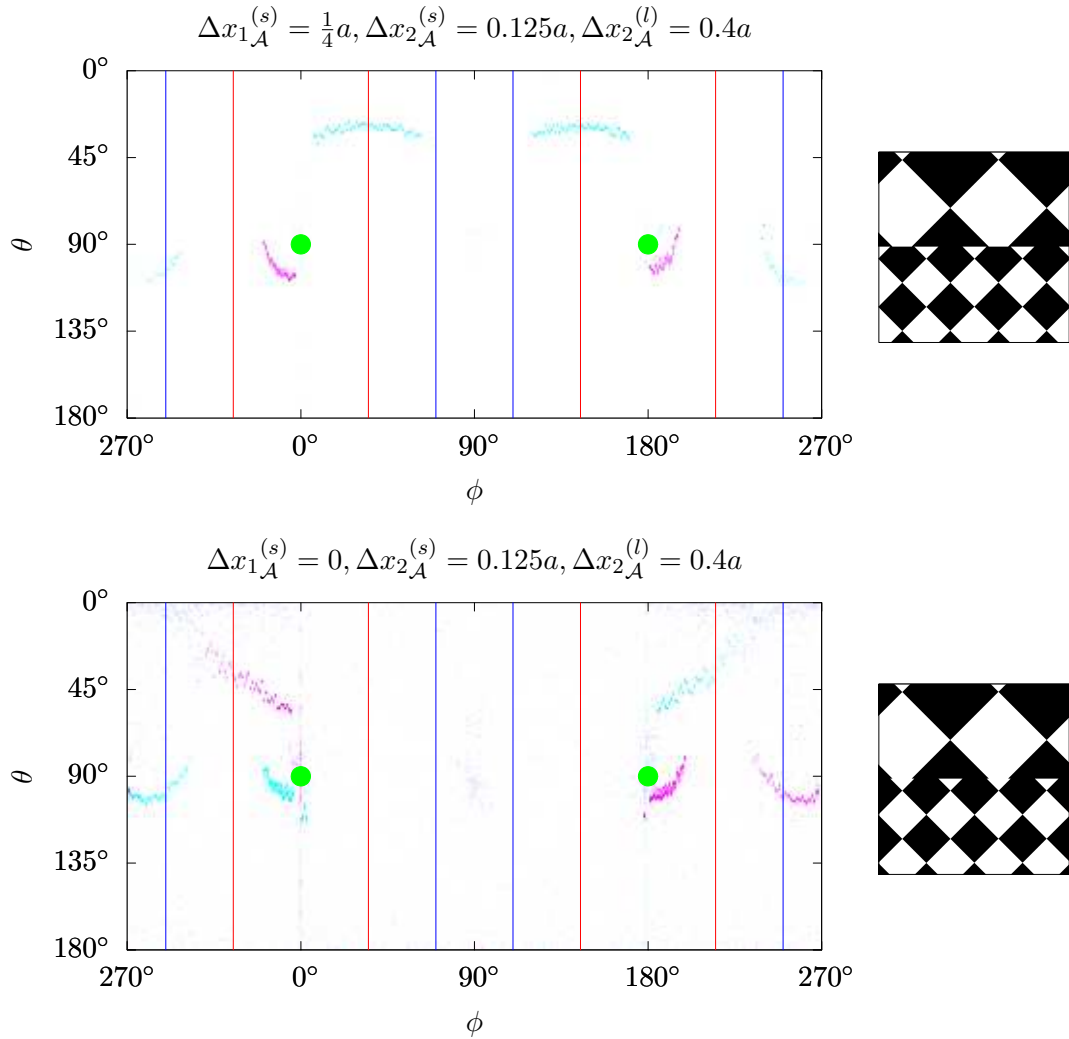


Figure 6.19: Fences in control space for two different symmetric patterns, symmetric to a plane perpendicular to the edge at $\phi = 90^\circ$. In the first image the colors are symmetric as well, in the second they are inverse in the mirror image. The difference is that the first pattern has a non-alternating mirror plane for black where the particle starts, the second an alternating one. The bifurcation point lies approximately at $\Delta\phi = 60^\circ$, so it is encircled by one but not the other loop. As a result, the top pattern has the behavioral modes β_1 for $\Delta\phi = 35^\circ$ and β_2 for $\Delta\phi = 70^\circ$, the bottom one β'_1 (35°) and β'_3 (70°).

7 Conclusions

Doing the experiments and simulations on the four-fold edge patterns, we could observe and describe edge transport for a variety of loops. Using symmetry considerations we can explain the experimental results, the absence or presence of transport of the colloidal particles along the edge at the same time as other particles perform trivial motion in the bulk of the pattern. Nevertheless, the details of the edge transport are complex and are depending on the exact type of pattern and the bifurcation points wound around with the loops in control space, so there is no obvious way to determine the resulting motion. We found that the simulations based on Brownian dynamics match the experimental result closely and are a good instrument to further study the problem. Thus we have done simulations for a variety of patterns and loops and represented the results in phase diagrams. We can combine this information to a behavioral mode for every combination of a pattern and a set of fundamental loops, describing the edge transport behavior for any combination of these loops. Hence we could classify two different types of modes, symmetric and asymmetric modes, each showing similar behavior for the different palindrome cyclotron loops. Looking at the fences in control space for the motion across the edge, we could also see the topological nature of the edge. Using our findings, one should be able to use combinations of the loops to induce transport only for specific edges which could be used to create complex transport modes for multiple particles at different edges.

Results from this Master thesis have been published in “Edge transport at the boundary between topologically equivalent lattices” by Helena Massana-Cid, Adrian Ernst, Daniel de las Heras, Adam Jarosz, Maciej Urbaniak, Feliks Stobiecki, Andreea Tomita, Rico Huhnstock, Iris Koch, Arno Ehresmann, Dennis Holzinger and Thomas M. Fischer, *Soft Matter* **15**, 1539-1550 (2019).

8 Zusammenfassung

Wir arbeiten mit mikrometergroßen superparamagnetischen Kern-Schale-Teilchen über einem zweidimensionalen magnetischen Muster, das sich in einem externen Magnetfeld mit sich ändernder Orientierung befindet. Dadurch bewegen sich die Teilchen in Abhängigkeit von topologischen Invarianten, den Windungszahlen des Magnetfelds um bestimmte Punkte [11]. Dieser topologische Transport unterscheidet sich für Muster verschiedener Symmetrien, zum Beispiel Zwei-, Drei- oder Vierfachsymmetrie [12]. Davon abhängig bewegt sich das Teilchen entweder nur adiabatisch, d.h. das Teilchen befindet sich während der ganzen Bewegung in einem lokalen Minimum, oder es existieren Ratschen in der Bewegung. Diese werden ausgelöst wenn ein Minimum und ein Sattelpunkt aufeinandertreffen und sich vernichten, sodass sich das Teilchen entlang des Pfades des steilsten Abstiegs in das nächste Minimum bewegt. Die Kombination von zwei Mustern verschiedener Symmetrie kann zu besonderen Transporteffekten führen, wie zum Beispiel zu „skipping orbits“ falls man ein hexagonales mit einem Streifenmuster kombiniert [10]. Alternativ kann man auch zwei Muster kombinieren, welche sich nur durch ihre Gitterkonstante unterscheiden [13].

In dieser Arbeit untersuchen wir Muster, welche aus zwei vierfachsymmetrischen Mustern unterschiedlicher Gitterkonstanten kombiniert sind. Dabei ist eine Gitterkonstante doppelt so groß wie die andere (Kapitel 2). Dadurch existieren in einer Einheitszelle eines Musters doppelt so viele Minima wie in einem gleich großen Bereich des anderen. Das wird vor allem an der Kante zwischen beiden Mustern deutlich, weil man einem Minimum auf der einen Seite zwei Minima auf der anderen Seite zuordnen kann. Dadurch entsteht, trotz rein adiabatischem Transport beim vierfachsymmetrischen Muster, die Möglichkeit Ratschen zu erzeugen. Durch geeigneter Wahl der Modulation des externen Magnetfelds können wir Teilchen entlang der Kante bewegen, wobei die Teilchen die sich nicht an der Kante befinden triviale Bewegung beschreiben. Dadurch sind wir in unserer Wahl der Modulationen beschränkt, und nutzen daher „cyclotron loops“, die zu einer geschlossenen Bewegung abseits der Kante führen, oder „palindrome loops“, wobei die Modulation des Magnetfelds zeitumkehrinvariant sind und dadurch im adiabatischen Fall ebenfalls zu keiner Netto-Bewegung führen. Wir erklären die Bewegungen für die verschiedenen Modulationen anhand von Symmetrieargumenten und unterstützen unsere Theorie mit Hilfe von Experimenten und Simulationen. Die Experimente werden mit paramagnetischen Teilchen auf einem dünnen magnetischen Muster durchgeführt, wobei das externe Magnetfeld computergestützt von drei Spulen erzeugt wird (Kapitel 3). Die Simulation wird mit Brownscher Dynamik durchgeführt, wobei das Teilchenpotential vom externen Magnetfeld und vom Magnetfeld des Musters an der Stelle des Teilchens abhängt (Kapitel 4, Kapitel 5). Wir sind so auch in der Lage, systematisch viele verschiedene Muster auszuprobieren da unser Muster aufgrund der Kante von drei unabhängigen Pa-

parametern bestimmt wird. Außerdem können wir so auch den topologischen Aspekt zeigen und Bifurkationspunkte identifizieren, da die Simulation das automatische Probieren von verschiedenen Modulationen ermöglicht. Die Experimente wurden in Zusammenarbeit mit Helena Massana-Cid durchgeführt, die unsere Arbeitsgruppe von der Universität Barcelona aus besuchte.

Die experimentellen Ergebnisse lassen sich vollständig mit Symmetrieargumenten erklären, allerdings lässt sich dadurch die Bewegung entlang der Kante nicht vollständig voraussagen. Die Simulation tut dies hingegen und stimmt mit den Experimenten überein (Kapitel 6). Die Ergebnisse zeigen, dass der Transport der Teilchen in komplexer Weise von der Wahl der Muster-Parameter als auch von der gewählten Modulation abhängen. Wir haben deshalb Phasendiagramme erstellt, um den Teilchentransport in Abhängigkeit dieser Variablen zu visualisieren. Das Verhalten für verschiedene Modulationen lässt sich auch zusammenfassen, sodass wir „Verhaltens“-Moden definieren können. Diese lassen sich wiederum in symmetrische und asymmetrische Moden unterteilen, welche sich jeweils ähnlich verhalten. Erwartungsgemäß finden wir durch Variation der Modulation des externen Felds in der Simulation auch die Bifurkationspunkte für ein bestimmtes Muster.

Bibliography

- [1] D. G. Grier, A revolution in optical manipulation. *Nature* **424**, 810 (2003).
- [2] S.-H. Lee and D. G. Grier, One-dimensional optical thermal ratchets. *J. Phys. Condens. Matter* **17**, S3685 (2005).
- [3] A. Erbe, M. Zientara, L. Baraban, C. Kreidler and P. Leiderer, Various driving mechanisms for generating motion of colloidal particles. *J. Phys. Condens. Matter* **20**, 404215 (2008).
- [4] J. F. Brady, Particle motion driven by solute gradients with application to autonomous motion: continuum and colloidal perspectives. *J. Fluid Mech.* **667**, 216–259 (2011).
- [5] H.-R. Jiang, N. Yoshinaga and M. Sano, Active motion of a janus particle by self-thermophoresis in a defocused laser beam. *Phys. Rev. Lett.* **105**, 268302 (2010).
- [6] J. Palacci, S. Sacanna, A. P. Steinberg, D. J. Pine and P. M. Chaikin, Living crystals of light-activated colloidal surfers. *Science* 1230020 (2013).
- [7] H. Massana-Cid, F. Martinez-Pedrero, E. Navarro-Argemí, I. Pagonabarraga and P. Tierno, Propulsion and hydrodynamic particle transport of magnetically twisted colloidal ribbons. *New J. Phys.* **19**, 103031 (2017).
- [8] P. Tierno, T. H. Johansen and T. M. Fischer, Localized and delocalized motion of colloidal particles on a magnetic bubble lattice. *Phys. Rev. Lett.* **99**, 038303 (2007).
- [9] S.-H. Song, H.-L. Lee, Y. H. Min and H.-I. Jung, Electromagnetic microfluidic cell labeling device using on-chip microelectromagnet and multi-layered channels. *Sens. Actuator B Chem.* **141**, 210–216 (2009).
- [10] J. Loehr, D. de las Heras, A. Jarosz, M. Urbaniak, F. Stobiecki, A. Tomita, R. Huhnstock, I. Koch, A. Ehresmann, D. Holzinger and T. M. Fischer, Colloidal topological insulators. *Commun. Phys.* **1**, 4 (2018).
- [11] J. Loehr, M. Loenne, A. Ernst, D. de Las Heras and T. M. Fischer, Topological protection of multiparticle dissipative transport. *Nat. Commun.* **7**, 11745 (2016).
- [12] J. Loehr, D. de las Heras, M. Loenne, J. Bugase, A. Jarosz, M. Urbaniak, F. Stobiecki,

Bibliography

- A. Tomita, R. Huhnstock, I. Koch, A. Ehresmann, D. Holzinger and T. M. Fischer, Lattice symmetries and the topologically protected transport of colloidal particles. *Soft matter* **13**, 5044–5075 (2017).
- [13] H. Massana-Cid, A. Ernst, D. de las Heras, A. Jarosz, M. Urbaniak, F. Stobiecki, A. Tomita, R. Huhnstock, I. Koch, A. Ehresmann, D. Holzinger and T. M. Fischer, Edge transport at the boundary between topologically equivalent lattices. *Soft Matter* **15**, 1539–1550 (2019).
- [14] P. Kuświk, A. Ehresmann, M. Tekielak, B. Szymański, I. Sveklo, P. Mazalski, D. Engel, J. Kisielewski, D. Lengemann, M. Urbaniak et al., Colloidal domain lithography for regularly arranged artificial magnetic out-of-plane monodomains in Au/Co/Au layers. *Nanotechnology* **22**, 095302 (2011).
- [15] M. Urbaniak, P. Kuświk, Z. Kurant, M. Tekielak, D. Engel, D. Lengemann, B. Szymański, M. Schmidt, J. Aleksiejew, A. Maziewski et al., Domain-wall movement control in Co/Au multilayers by He⁺-ion-bombardment-induced lateral coercivity gradients. *Phys. Rev. Lett.* **105**, 067202 (2010).
- [16] J. Quispe-Marcatoma, B. Pandey, W. Alayo, M. De Sousa, F. Pelegrini and E. B. Saitovitch, Preferential orientation of magnetization and interfacial disorder in Co/Au multilayers. *J. Magn. Magn. Mater.* **344**, 176–181 (2013).
- [17] J. Jackson, C. Witte, M. Diestelhorst and K. Müller, *Klassische Elektrodynamik*. De Gruyter (2013).
- [18] M. Matsumoto and T. Nishimura, Mersenne twister: a 623-dimensionally equidistributed uniform pseudo-random number generator. *ACM Trans. Model. Comput. Simul.* **8**, 3–30 (1998).
- [19] D. de las Heras, J. Loehr, M. Loenne and T. M. Fischer, Topologically protected colloidal transport above a square magnetic lattice. *New J. Phys.* **18**, 105009 (2016).

Erklärung

Hiermit bestätige ich, dass ich die vorliegende Arbeit selbst verfasst, nur die angegebene Literatur als Hilfsmittel verwendet habe und alle wörtlich oder sinngemäß übernommenen Äußerungen anderer Autoren gekennzeichnet habe. Außerdem versichere ich, dass ich die Arbeit zu keinem früheren Zeitpunkt bereits zur Erlangung eines akademischen Grades eingereicht habe.

Bayreuth, den 26. Februar 2019

ADRIAN ERNST